Journal of Nanomaterials

Hydrodynamic and Thermal Advancements in the Fundamentals and Applications of Nanofluids

Lead Guest Editor: Hafiz Muhammad Ali
Guest Editors: Chi Chuan Wang and Josua Meyer

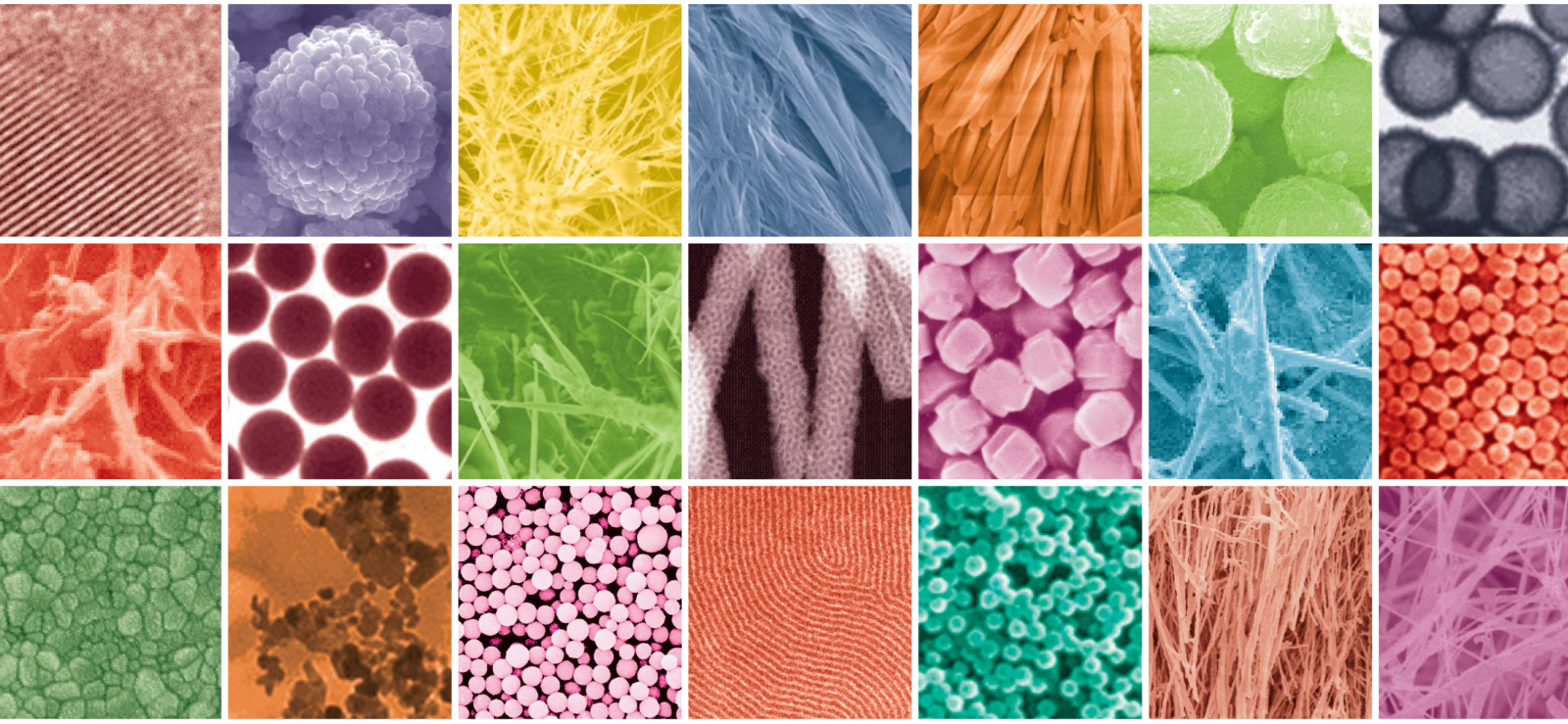

Hydrodynamic and Thermal Advancements in the Fundamentals and Applications of Nanofluids

Journal of Nanomaterials

Hydrodynamic and Thermal Advancements in the Fundamentals and Applications of Nanofluids

Lead Guest Editor: Hafiz Muhammad Ali
Guest Editors: Chi Chuan Wang and Josua Meyer

Contents

Hindawi
Journal of Nanomaterials
Volume 2022, Article ID 3530419, 17 pages
https://doi.org/10.1155/2022/3530419

Research Article

Thermal Analysis of Graphene-Based Nanofluids for Energy System and Economic Feasibility

Reem Sabah Mohammad,[1] Mohammed Suleman Aldlemy,[2] Ali M. Ahmed,[3] Mayadah W. Falah,[4] Sumaiya Jarin Ahammed,[5] and Zaher Mundher Yaseen[6]

[1]*University of Misan, Kahla Road, Misan, Iraq*
[2]*Department of Mechanical Engineering, College of Mechanical Engineering Technology, Benghazi, Libya*
[3]*Engineering Department, Al-Esraa University College, Baghdad, Iraq*
[4]*Building and Construction Techniques Engineering Department, Al-Mustaqbal University College, Hillah, Babylon 51001, Iraq*
[5]*International University of Business Agriculture and Technology, Dhaka, Bangladesh*
[6]*Civil and Environmental Engineering Department, King Fahd University of Petroleum and Minerals, Dhahran 31261, Saudi Arabia*

Correspondence should be addressed to Sumaiya Jarin Ahammed; star.dust227@gmail.com

Received 21 June 2022; Revised 16 August 2022; Accepted 8 September 2022; Published 12 October 2022

Academic Editor: Hafiz Muhammad Ali

Graphene has piqued the interest of many researchers due to its superior mechanical, thermal, and physiochemical properties. Graphene nanoplatelets with covalently functionalized surfaces (CF-GNPs) were employed in turbulent-heated pipes to undertake thermal and economic studies. CF-GNPs and distilled water were used to make the current nanofluids at various mass percentages, such as 0.025, 0.05, 0.075%, and 0.1 wt.%. In the range of 6,401 Re 11,907, the thermal system was heated up to 11,205 W/m^2 under fully developed turbulent flow conditions. Field emission scanning electron microscopy (FE-SEM), zeta potential, nanoparticle sizer, and field emission transmission electron microscopy (FE-TEM) were used to examine the morphological features and characterise the particles. In addition, the current thermal system's economic performance was assessed to estimate its price-to-operate ratio. There was a 16.10% reduction in heat exchanger size for 0.025 weight percent, 0.05 weight percent, 0.075 weight percent, and 0.1 weight percent. In addition, the power needed for the base fluid was 422 W, which was then lowered to 354 W, 326 W, 315 W, and 298 W for 0.025 wt.%, 0.05 wt.%, 0.075 wt.%, and 0.1 wt.%, respectively.

1. Introduction

1.1. Research Background and Motivation. The essential demand for high-performance heat transfer fluids in various applications and industries, particularly in the energy and electrical sectors, has motivated much research [1, 2]. Heat transfer efficiency is low in many engineering applications due to using low-conductive fluids such as water- and oil-based fluids [3–5]. As a result, researchers seek an alternate mechanism to replace these traditional fluids to improve thermal transfer efficiency. "Nanofluids" are solid nanoparticles (NPs) suspended in base fluids in a long-stable and homogeneous approach [6–8]. Nanofluids have previously been shown to improve heat transfer efficiency in a variety of engineering applications [9], including heat exchangers [10], heating/cooling systems [11], and solar panel appliances [6]. As a result, new conductive fluids containing various nanoparticles have been developed, such as metal oxides (Al_2O_3, ZnO, CuO, SiO_2, and TiO_2) [12–14], and carbon-based nanofluids (MWCNTs, GO, and GNPs) [15–17].

1.2. Adopted Literature Review on Nanofluids-Based Heated Pipe. The varied features of graphene have attracted much research interest [18]. Graphene is a carbon allotrope composed of a single layer of hexagonally-organised carbon atoms that are sp^2 bonded [19]. Exfoliated graphene nanoplatelets (GNPs) are a new type of graphite nanoparticle

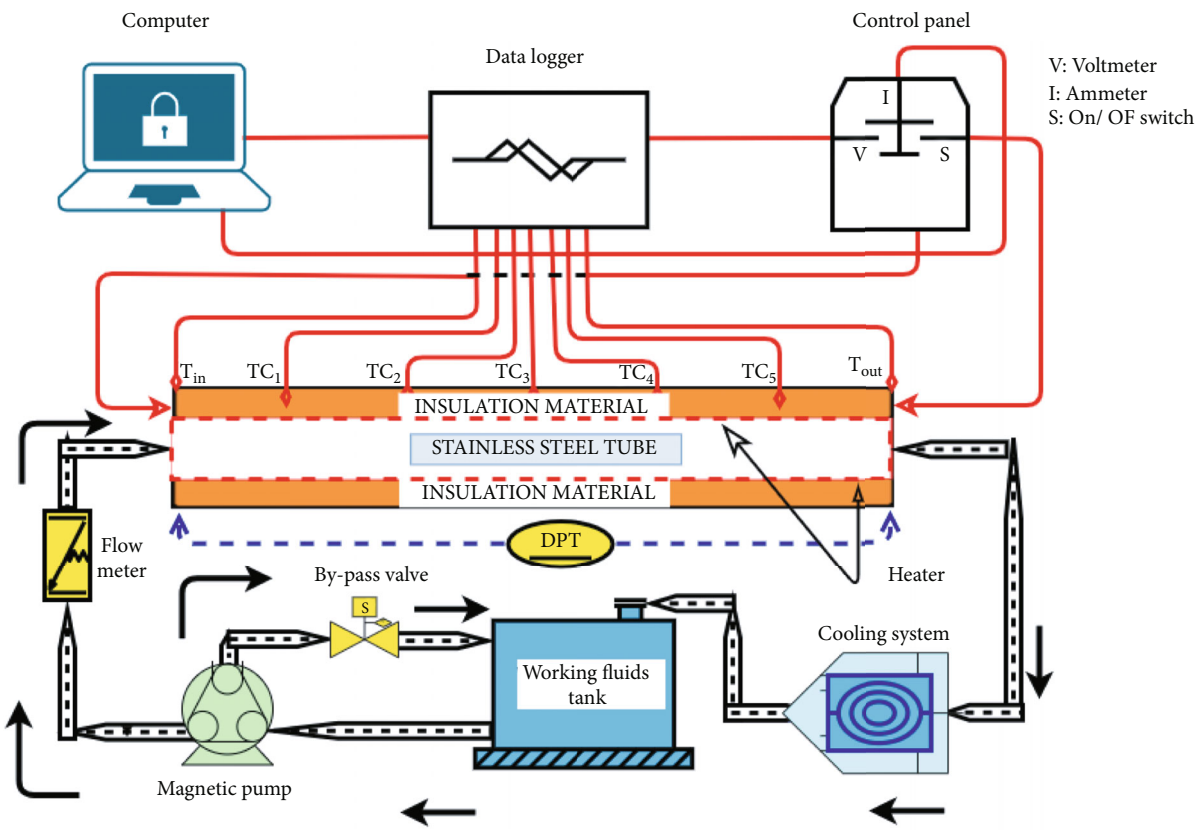

Figure 1: Drawing diagram for the forced convective heat transfer in turbulent flow.

made up of microscopic flakes of graphene that are around 1-15 nm thick and with sizes ranging from submicrometers to 100 micrometers [20, 21]. GNPs are a fantastic nanomaterial from an economic standpoint because they can be manufactured at a minimal cost [22]. On the other hand, graphene nanoplatelets have a problem with solubility in solution because they prefer to collect under the influence of strong Van der Waals forces [23]. Different techniques and tactics for chemically functionalizing the surface of GNPs have been developed to address the solubility issue [24–26].

The graphene surface can be changed using two basic strategies: covalent functionalization (rapid insertion of functional groups on the graphite surface) and strong attachment of surfactants to increase dispersion (noncovalent functionalization) [27, 28]. The noncovalent approach creates polar-polar linkages by coating the graphene surface with surfactants or polymers that act as stabilizers to prevent GNPs from solidifying in homogenous liquids [29]. Stabilizers are inconvenient since they can contaminate GNPs and lower their value [30]. Conversely, covalent functionalization necessitates binding with hydrophilic functional groups such as carbonyl, hydroxyl, carboxyl, sulfhydryl, amino, and phosphate groups [31]. Furthermore, altering the graphene structure is a viable option for increasing solubility in solvents and polymers [32]. To date, toxic substances such as high-risk acids have been used in chemical oxidation-reduction reactions to functionalize GNPs.

Table 1: Heat transfer and fluid flow parameters.

Parameter	Formula
Heat flux (q'')	$\frac{V \times I}{4D_h L}$
Heat transfer coefficient (h)	$\frac{q''}{T_w - T_b}$
Nusselt number (nu)	$\frac{hD_h}{k}$
Friction factor (f)	$\frac{\Delta P}{(L/D)(\rho v^2/2)}$
Reynolds number (re)	$\frac{4\dot{m}}{\pi D_h \mu}$
Prandtl number (Pr)	$\frac{\mu C_p}{k}$

The production of functionalized GNPs for various applications (such as fluids in heat exchangers and some other heating and cooling applications) has been considered by numerous scholars. For instance, the study by Wang et al. [33] used GNP nanofluids to investigate laminar flow in the presence of an unidentified surfactant at 1 wt.%. An increase in pressure drop was observed using the GNP nanofluid as the flow rate increased, reaching approximately three times that of pure water. It was also observed that the interaction between the nanoparticles and the viscosity forces within

Table 2: Ranges and precisions of tools and working fluid properties.

Instrument/sensor	Range	Uncertainty
Type-T thermocouple	0-300°C	±0.1 °C
RTD (PT-100) sensor	0-200 °C	±0.1 °C
Burkert flow meter (type SE32)	0.3-10 m/s	±1%
Differential pressure transmitter (PX154-025DI)	0-6.23 kPa	±0.75%
Power supply	0-260 V	0.33 V
	0-12 A	0.04 A
Thermal conductivity	0.2-2 W/m. K	5%
Dynamic viscosity	−150 to + 1000°C	1%
Density	0-3 g/cm^3	1%
Specific heat	0.01°C to 300°C/min	2%

Table 3: Heat transfer and fluid flow uncertainties [47].

No.	Parameter	Uncertainty formulas	Uncertainty values
1	Reynolds number (re)	$\frac{U_{Re}}{Re} = \sqrt{\left(\frac{U_\rho}{\rho}\right)^2 + \left(\frac{U_{\bar{V}}}{\bar{V}}\right)^2 + \left(\frac{U_\mu}{\mu}\right)^2}$	±1.73%
2	Heat flux (q ")	$\frac{U_q}{q} = \sqrt{\left(\frac{U_V}{V}\right)^2 + \left(\frac{U_I}{I}\right)^2}$	±1.51%
3	Heat transfer coefficient (h)	$\frac{U_h}{h} = \sqrt{\left(\frac{U_q}{q}\right)^2 + \left(\frac{U_{(T_w - T_b)}}{(T_w - T_b)}\right)^2}$	±1.52%
4	Nusselt number (nu)	$\frac{U_{Nu}}{Nu} = \sqrt{\left(\frac{U_h}{h}\right)^2 + \left(\frac{U_k}{k}\right)^2}$	±5.23%
5	Friction factor (f)	$\frac{U_f}{f} = \sqrt{\left(\frac{U_{\Delta p}}{\Delta p}\right)^2 + \left(\frac{U_\rho}{\rho}\right)^2 + \left(\frac{U_{\bar{V}}}{\bar{V}}\right)^2}$	±1.60%

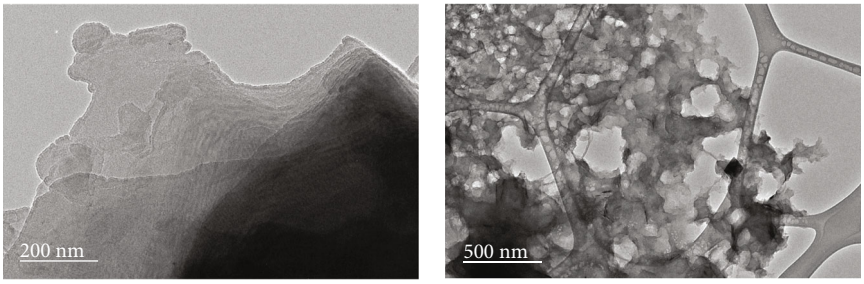

(a) (b)

Figure 2: HR-TEM microscopy at different magnifications (a) pristine GNPs and (b) CF-GNPs.

the particle caused a significant decline in Nu_{avg} (more slowly than water) as the axial distance increased. Alawi et al. [34] tested PEG-TGr in a heated 10 mm internal diameter square pipe system. The mass fraction ranged from 0.025, 0.05, 0.075, and 0.1 wt.%, while the Re ranged from 6,400 to 11,900 at a heat flow rate of 11,205 W/m^2. There was a steady improvement in the convective heat transfer coefficient by up to 41.2%.

Furthermore, the friction factor increased by 3.8% at Re = 11,900, while the pressure decreased by up to 22.3%. A slight reduction in concentration affected the heat transfer minimally as the coefficient of heat transfer improved by 28.8% at 0.025 wt.%. Examination of the pressure loss and heat transfer properties was done using circular and square heat pipes in the presence of Al_2O_3 and SiO_2 (two metallic oxides), as well as KRG and GNPs (two carbon-based nanostructured nanofluids) [35]. Among the studied working fluids, DW had the best performance index, while the nanofluids (at the lowest concentration but excluding KRG/DW) exhibited the best index for that nanofluid. P-GNPs were

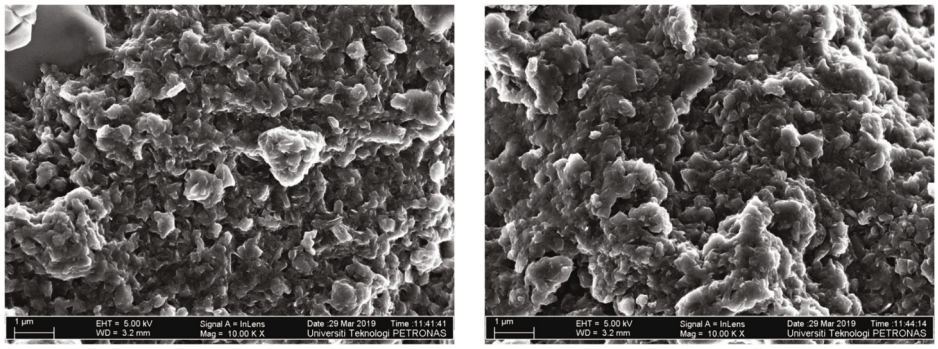

(a) (b)

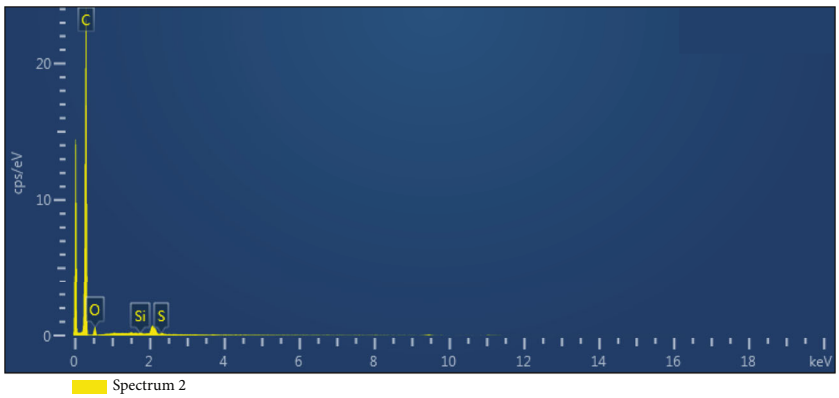

(c)

Spectrum 2				
Element	Line type	Weight %	Weight % sigma	Atomic %
C	K series	90.28	0.35	92.59
O	K series	9.53	0.35	7.33
Si	K series	0.09	0.02	0.04
S	K series	0.10	0.03	0.04
Total		100.00		100.00

(d)

Figure 3: SEM and EDX analysis of the CF-GNPs nanoparticles: (a–b) SEM at 1 μm; (c) EDX mapping analysis; (d) EDX elemental analysis.

examined by Montazer [36] in a 12.7 mm and 25.4 mm sudden expansion configuration at an expansion ratio of 2. The heat flow was 12,129 W/m^2, and the Re varied from 4,000 to 16,000. The heat transfer coefficient increased by around 33.7% at one point. The convective heat transfer coefficient was significantly improved, but the relative pumping power increased only a little by 33.05 and 1.19%, respectively [37]. More importantly, the observed good performance index indication for all Reynolds number ranges indicates that the synthesized MWCNTs aqueous suspensions might be used as an alternate working fluid in heat transfer systems.

1.3. Research Objectives. There has been a lot of research interest due to the increased need for technology that can accelerate heat transfer in heating and cooling systems. After much study in this area, it is necessary to investigate whether nanofluids can significantly alter heat transfer to satisfy specialists' expectations in the field. There is a demand for a cost-effective and reliable technique to prepare covalently functionalized graphene nanoplatelets (CF-GNPs) for convective heat transfer applications. The main objective of this work is to investigate methods for improving the thermal performance of CF-GNPs-H_2O nanofluid under fully developed turbulent flow conditions. The thermophysical and surface modifications properties of the synthesized CF-GNPs were investigated at various measuring conditions. Also, economic and thermal analyses were performed, such as heat exchanger size reduction, energy savings, and the total cost of thermal system operation.

2. Methodology

2.1. Materials and Functionalization Approach. GNPs were made using raw materials that met the following requirements: 2 m, SSA = 750 m^2/g, and 98% purity (were purchased from XG Sciences, Lansing, MI, USA). Additionally, the primary chemicals, such as nitric acid (HNO_3; 65%) and sulfuric acid (H_2SO_4; 95–97%), were acquired from a local Malaysian company for chemicals supplies (Sigma-Aldrich Co., Selangor, Malaysia).

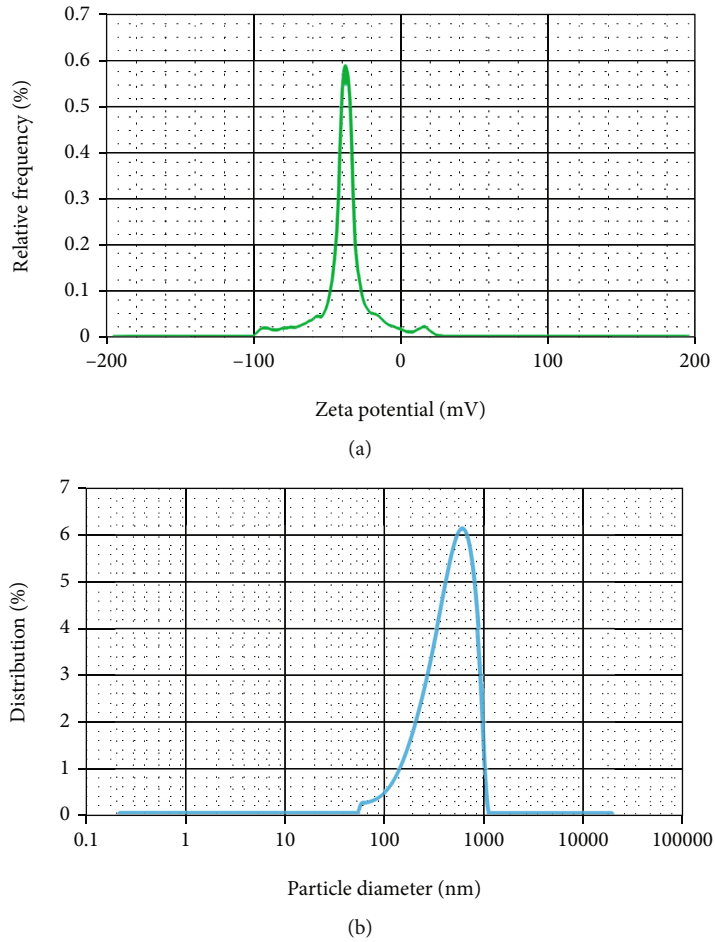

Figure 4: (a) Zeta potential values of CF-GNP nanofluids and (b) particle size distributions for CF-GNPs at 25°C.

In the first process, the raw materials GNPs were dispersed in the functionalization medium containing HNO_3 (67%) and H_2SO_4 (98%) at a mixing ratio of 1:3 [38]. Then, the sample was transferred into H_2SO_4 with mild shaking. One gram of the pristine GNPs (P-GNPs) was added into a flask with 250 mL containing the oxidation agent before being placed in an iced bath. Then, a few drops of nitric acid were added to the mixture, and the solution was stirred at room temperature for 30 min. Then, an ultrasonication bath was applied for 3 hrs to the black product. Also, further reflux for 30 mins was performed at room temperature. The washing process was applied at the speed of 6,000 rpm for 15 minutes before using the dryer at 80°C for 24 hours using DW until the pH value reached 5. In the last step, four different mass fractions were prepared as 0.025, 0.05, 0.075, and 0.1 wt.% as heat transfer working fluids in the current investigations.

2.2. Experimental Measurements. Adding CF-GNPs nanoparticles to the base fluid (DW) increases/decreases nanofluids' thermal-physical properties (thermal conductivity, viscosity, density, and specific heat). The new values of nanofluids' thermal-physical properties show implications for heat transfer and fluid flow in thermal applications. In this regard, the device (KD-2 pro, Decagon, USA) was used to measure the base fluid and nanofluids' thermal conductivity in the temperature range of 0-60°C with an average accuracy of 5% [39]. The device measurements were validated with the published data of DW. The dynamic viscosity of DW and GNPs-DW nanofluids was measured by using the device of (Rheometer, Physica, MCR 301, Anton Paar, Austria). Also, the specific heat capacity and density of DW and GNPs-DW were assessed using DSC 8000 (Perkin Elmer, USA) and (Mettler Toledo) DE-40 with the accuracy of ±2% and $\pm 10^{-4}$ g/cm^3, respectively. The average errors between the measurements and published data were 3.3%, 4.45%, 3.13%, and 2.46% for thermal conductivity, dynamic viscosity, density, and specific heat, respectively. Two types of electron microscopy were used to examine the morphological parameters (size and form) of the synthesized nanoparticles/nanofluids. These include field emission transmission (FE-TEM, JEM-2100F) and field emission scanning (FE-SEM, JEM-2100F) (FE-SEM, Zeiss Supra 55VP). In the meantime, the long-term stability was assessed using (Anton Paar, Litesizer 500, Austria).

Figure 1 displays the schematic drawing of the experimental setup used in the current study. The heating system generally includes the heated pipe (test section) with different measuring and controlling tools, a data logger device,

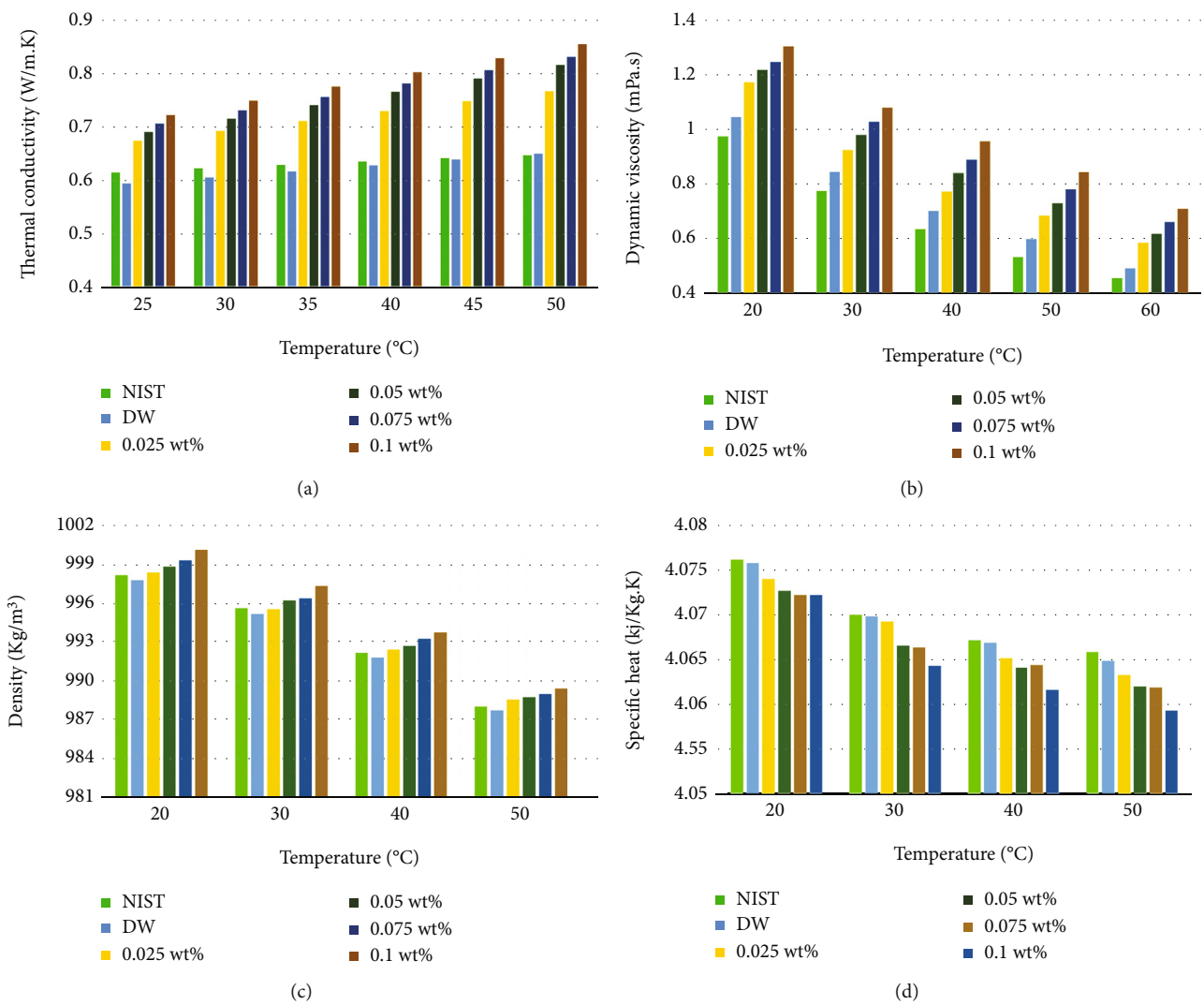

Figure 5: Thermal-physical properties of CF-GNPs versus mass fraction and temperature: (a) thermal conductivity, (b) dynamic viscosity, (c) density, and (d) specific heat capacity.

and a chiller compartment. The heat transfer fluid (sample) was pumped using a magnetic drive pump (Cole-Parmer™) at 0-10 liter/m flow rate from a stainless-steel jacket tank (12-liter capacity). The desired flow rate for base fluid and nanofluids was controlled by (Burkert Flow Meter, Type SE32). Meanwhile, the pressure inlet and pressure outlet along the heated-pipe test sections were measured by differential pressure transmitter (PX154-025DI, OMEGA) with an accuracy of ±0.75%.

1.4 m long, 10 mm wide inside, and 12.8 mm wide on the outside is used as the test section. The heating source is a 900 W flexible tape heater (OMEGA, USA) with an adjustable transformer. Also, the insulation is applied using thick glass wool to limit the heat loss to the surroundings. Five Omega T-type thermocouples were placed to get an accurate reading of the surface temperature of 0.1°C. Moreover, two RTD-sensors (PT-100) with an error of ±0.1°C were put into the inlet and outlet flow to measure the bulk temperature. The working fluids container was coupled to a chiller (DAIHAN-brand, WCR-P30) to keep the desired input temperature at 30°C.

2.3. Data Reduction and Uncertainties. Before moving on to the CF-GNPs-DW nanofluids, a water run was carried out to calibrate the system. The data was collected once the steady-state conditions had been achieved, such as the experiment's input, outlet, and heated surface temperatures. Methodologies used in this work to establish the most important parameters for evaluating thermal performance and nanofluid flow are shown in Table 1.

Here, $T_w = \sum T/5$ (T_w = the average temperature of the heated − wall surface), P = the wetted perimeter, $T_b = T_o - T_i/2$, $D_h = 4A_c/P$, and A_c = the cross − sectional area [40].

The maximum error between the heat supplied to the system $(Q = V \times I)$ and the heat gained by the working fluid $(Q = \dot{m}C_p[T_o - T_i])$ was ±7.2%, which acknowledges a minor percentage of heat loss to the room ambiance.

Here are some of the Nusselt number correlations that are currently available:

The single-phase fluids formula of Petukhov [41] was modified by Gnielinski [42]:

$$\mathrm{Nu} = \frac{(f/8)(\mathrm{Re}-1000)\mathrm{Pr}}{1+12.7(f/8)^{0.5}\left(\mathrm{Pr}^{2/3}-1\right)}\left[1+\left(\frac{d}{L}\right)^{2/3}\right]\left(\frac{\mathrm{Pr}_m}{\mathrm{Pr}_w}\right)^{0.11}. \tag{1}$$

Here, the Gnielinski equation is only applicable in the ranges of $3{,}000 < \mathrm{Re} < 5\times10^6$ and $0.5 < \mathrm{Pr} < 2{,}000$. Pr_m and Pr_w refer to the Prandtl number at bulk and wall temperatures, respectively.

According to Equation (2), the friction factor for a fully developed turbulent flow was determined depending on Re number by applying the Colebrook formula as follows: [43]

$$\frac{1}{\sqrt{f}} = -2.0\log\left(\frac{\varepsilon/D}{3.7}+\frac{2.51}{\mathrm{Re}\sqrt{f}}\right). \tag{2}$$

Meanwhile, the turbulent flow formula of Petukhov is shown in Equation (3)

$$\mathrm{Nu} = \frac{(f/8)\mathrm{RePr}}{1.07+12.7(f/8)^{0.5}\left(\mathrm{Pr}^{2/3}-1\right)}. \tag{3}$$

Here, Petukhov formula is valid for $0.5 < \mathrm{Pr} < 2000$ and $3000 < \mathrm{Re} < 5\times10^6$. Also, the Blasius and Petukhov correlations were employed to verify the water run test results [41, 44, 45].

$$f = (0.79\ln(\mathrm{Re})-1.64)^{-2}, \tag{4}$$

$$f = \frac{0.316}{\mathrm{Re}^{0.25}}. \tag{5}$$

For more evaluation, the thermal performance index (PI) and performance evaluation criteria (PEC) are determined to describe the desired output enhancement (heat transfer performance) over the unwanted output enhancement (pumping power) of CF-GNPs-H_2O nanofluids [46]:

$$\mathrm{PI} = \frac{h_{nf}/h_{bf}}{\Delta P_{nf}/\Delta P_{bf}} = \frac{R_h}{R_{\Delta P}},$$
$$\mathrm{PEC} = \frac{Nu_{nf}/Nu_{bf}}{\left(f_{nf}/f_{bf}\right)^{1/3}}, \tag{6}$$

where (R_h) and ($R_{\Delta P}$) indicate the ratio of heat transfer enhancement (nanofluid/DW) to the pressure loss increments (nanofluids/DW). When the value of (PI) and (PEC) is more than 1, the CF-GNPs-DW nanofluids can be effectively used in the square heated-pipe instead of the distilled water as HTFs. Meanwhile, when the PI and PEC < 1, the CF-GNP nanofluid is not a proper replacement.

Due to the many forms of faults, there is no such thing as an experiment that is 100% accurate. Some of these errors are accidental, while others result from egregious mistakes made by the experimenter or researcher. The problem may arise with the data that appears to be good, in which case the error analysis is crucial to confirm the validity of the data obtained experimentally or investigated analytically. The bad data may be discarded immediately because it does not require extensive experience to identify the errors of such data. Measurements of heat transfer, pressure drop, and nondimensional groups like Reynolds number and Nusselt number are all subjected to uncertainty and error analysis to confirm the current study's findings. Since the wall thermocouples cannot accurately measure the temperature at the surface of the heating pipe without obstructing the fluid flow, the thermocouples were placed a short distance from the heater wall. A Wilson plot was used in a calibration experiment to determine the temperature differential between the thermocouples and the wall surface. Table 2 shows the range and accuracies of instruments and fluid flow properties. While Table 3 [47] identified the uncertainties of all the values discussed.

2.4. Theory of Cost-Efficiency. The primary objective of this article is to compare the efficiency of nanofluids to their cost. The expense of manufacturing nanoparticles is well known. On the other hand, in addition to the expense of nanoparticles, the production of nanofluids is expensive. Basic fluid price is considered insignificant in the pricing of nanofluids. One of the generally used criteria for evaluating the effectiveness of nanofluids with the condition of turbulent flow is the Mouromtseff criterion [48, 49]. Under turbulent flow conditions, this criterion considers four characteristics of nanofluids: thermal conductivity, specific heat capacity, density, and dynamic viscosity. The Mouromtseff criteria is depicted in Equation (7). The Mouromtseff criteria shows that the efficiency of CF-GNPs in different mass percentages is higher than 1. The efficiency of CF-GNP nanofluids increases as mass percentages are increased. This means that, using CF-GNP nanofluids will save energy.

$$\mathrm{MO} = \left(\frac{\rho_{nf}}{\rho_{bf}}\right)^{0.8}\times\left(\frac{k_{nf}}{k_{bf}}\right)^{0.67}\times\left(\frac{Cp_{nf}}{Cp_{bf}}\right)^{0.33}\times\left(\frac{\mu_{nf}}{\mu_{bf}}\right)^{0.47}. \tag{7}$$

3. Results and Discussion

3.1. Characterization and Thermophysical Properties. Figures 2 and 3 showed the morphologies of P-GNPs and CF-GNPs via HR-TEM and FE-SEM examinations. As shown in Figure 2(a), P-GNP was composed of smooth surfaces, transparent structures, and dual sheets with intact edges. During the acid-based functionalization process, the carboxyl group (COOH) attachments on the surfaces and edges of the GNPs caused a slight blur effect with wrinkles and crumples on the sheets. The presence of defective folded flakes and rough edges, as seen in Figure 2(b), indicates a successful reaction between the GNPs-COOH and the acid

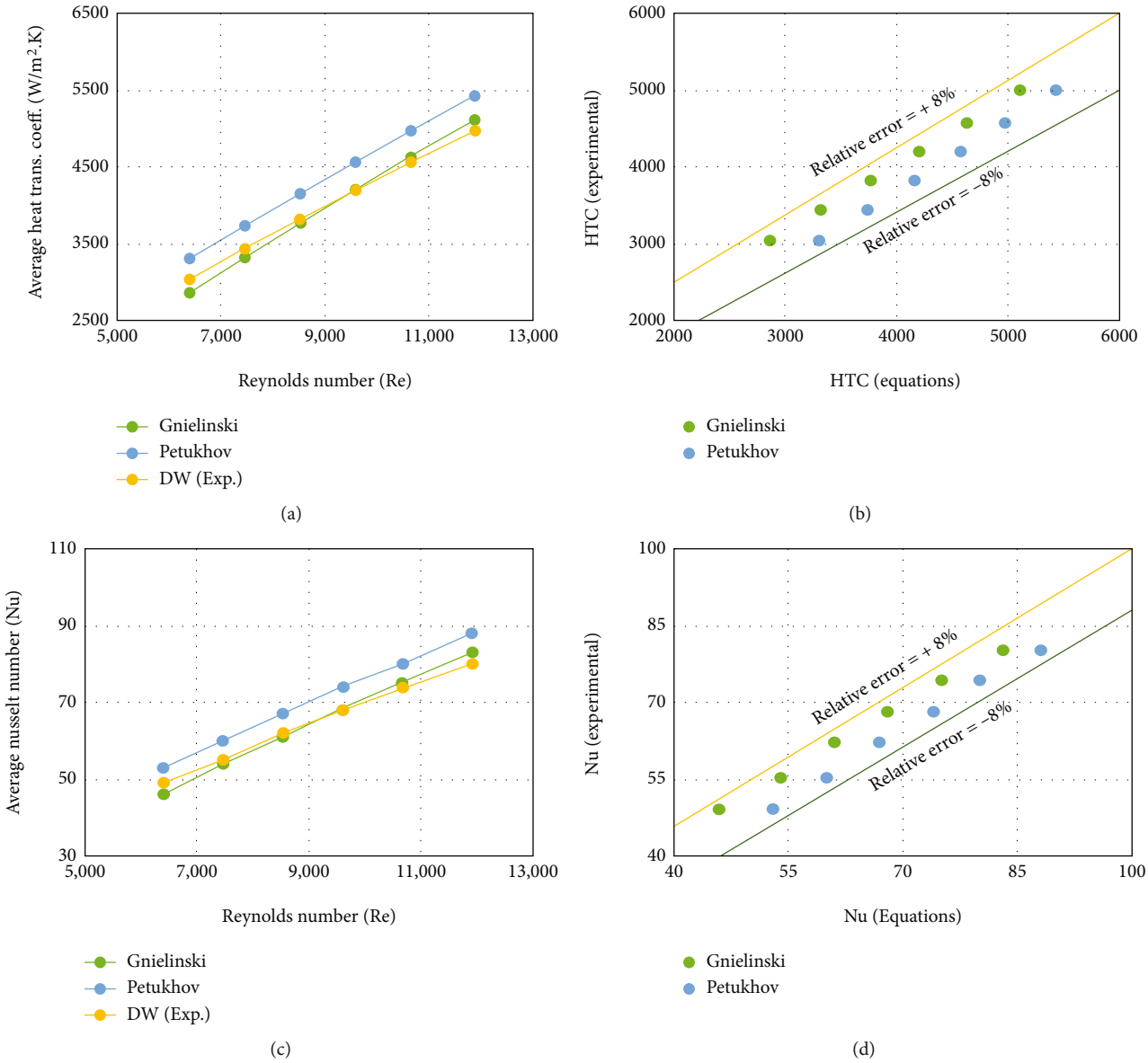

Figure 6: Continued.

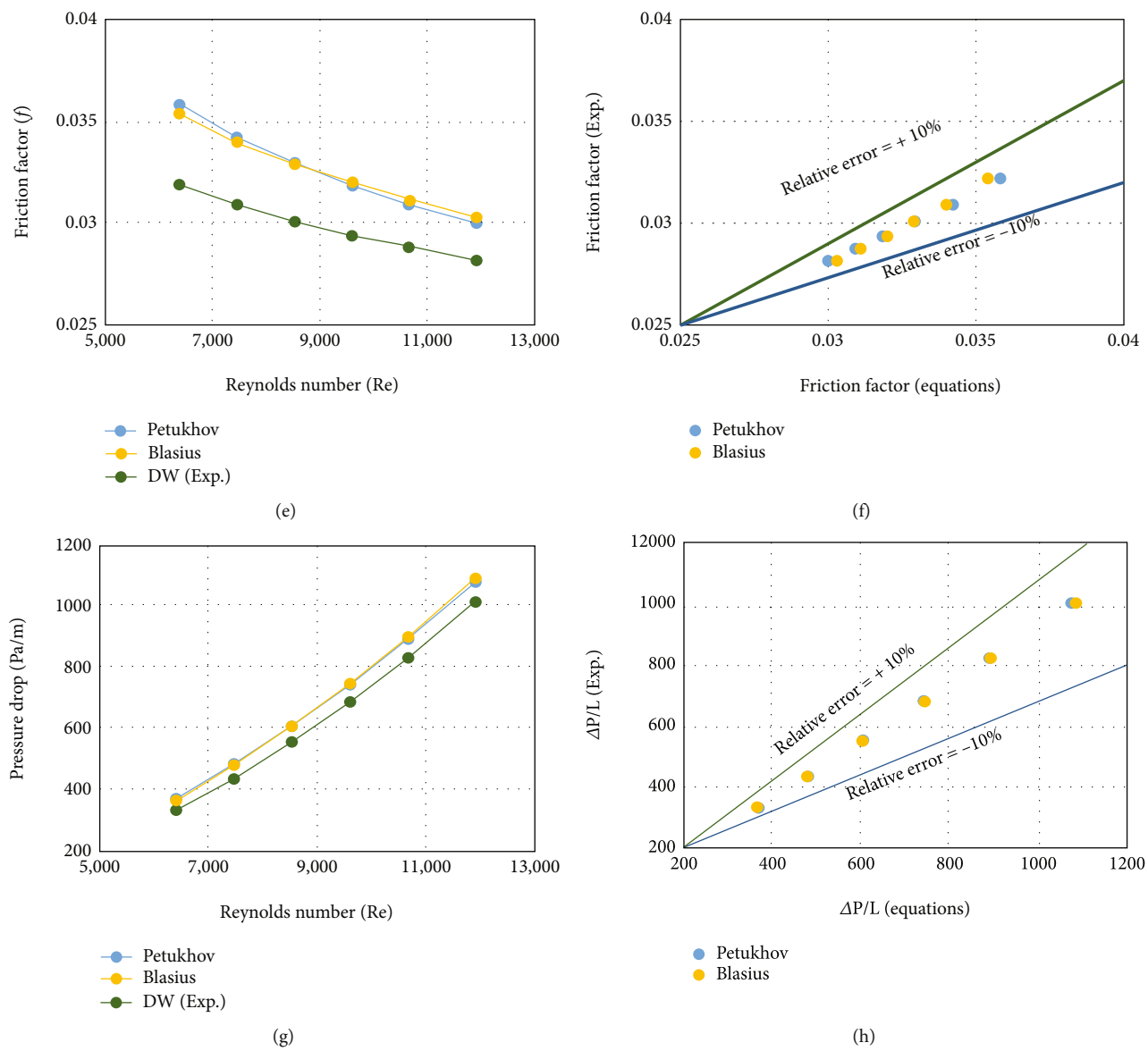

Figure 6: Validation and verification for water run: (a) heat transfer coefficients, (b) relative errors between measurements and equations, (c) average Nusselt number, (d) relative errors between measurements and equations, (e) Darcy friction factor, (f) relative errors between measurements equations, (g) pressure drop, and (h) relative errors between measurements and equations.

solution molecules. The wrinkles on the surface of GNPs are visible in HR-TEM pictures due to their inherent stability in 2D structures. These lines were more vital after the sonication-assisted chemical reactions than the previous wrinkling or surface roughness. Another observation from the FE-SEM microimages for the CF-GNP results in graphene nanoplatelets' fractured sheets is shown in Figures 3(a) and 3(b). The observations also agree with the results reported by [32, 38]. The energy-dispersive X-ray (EDX)-based spectra of the CF-GNPs are shown in Figures 3(c) and 3(d), with four elements (C, O, Si, and S) detected. The high carbon percentage (92.59%) indicates the success of the chemical reaction, and the presence of oxygen (7.33%) refers to the use of oxidizing acid. Furthermore, the silicon and sulphur contents were 0.04% and 0.04%, respectively.

The produced CF-GNP nanofluids' zeta potential and particle size distributions are illustrated in Figures 4(a) and 4(b), where Figure 5(a) shows the determined zeta potential and polydispersity index (PDI) of CF-GNPs-H_2O nanofluid at pH -7. The zeta potential must be as high as possible (+/-) to achieve a natural intraparticles repulsive force, as this would assure the existence of electrostatic repulsive forces between the CF-GNP nanoparticles. The experiments showed that the CF-GNPs exhibited a negative charge of -39.4 mV at 25°C within 1 hr sonication. The average size distribution of nanomaterials was determined using the dynamic light scattering (DLS) technique. The average particle size was calculated to be 447.3 nm (Figure 5(b). At the same time, the DLS results revealed that the particle size scale ranged from 51.6-121.6 nm with a low PDI of 0.306, indicating a consistent and uniform particle size distribution.

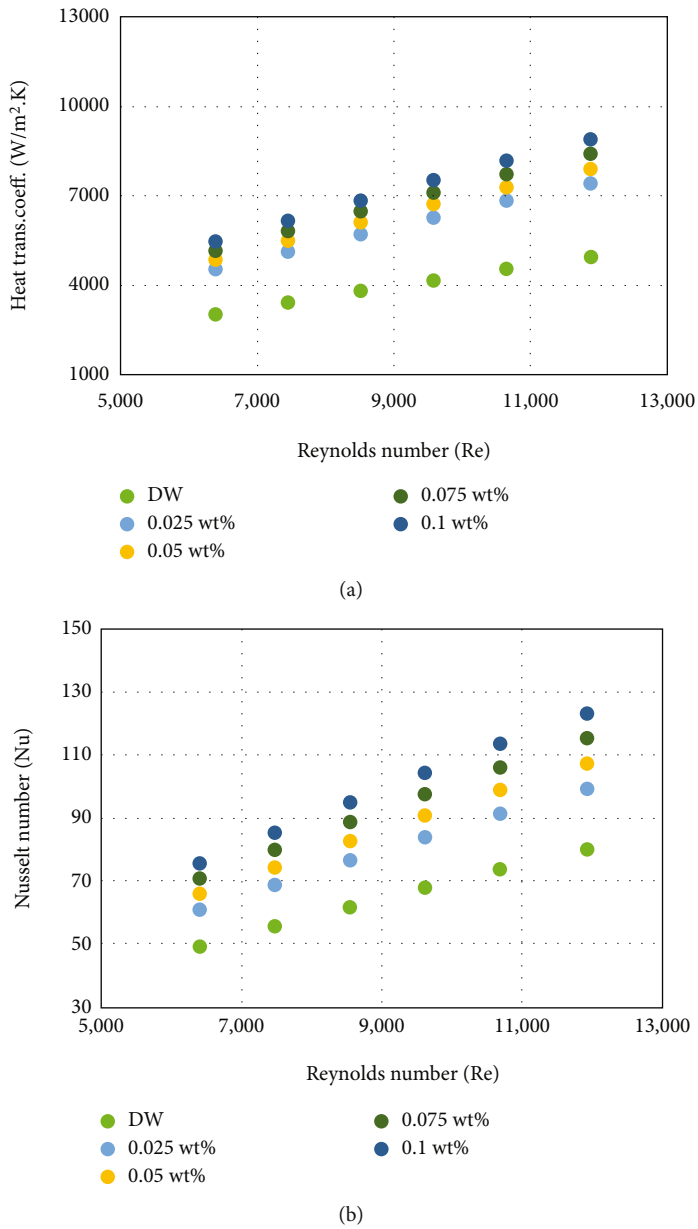

Figure 7: Heat transfer coefficients and average Nusselt number of CF-GNP nanofluids at various mass fractions against Reynolds number: (a) heat transfer coefficients; (b) average Nusselt number.

Figure 5 plots the thermal-physical properties of the DW and CF-GNPs-DW nanofluids against temperature and mass fractions of nanoparticles. The National Institute of Standards and Technology (NIST) database was used to validate the obtained thermal conductivity data with a maximum error of just 2% [50]. Figure 5(a) demonstrates a significantly higher thermal conductivity of CF-GNPs compared to DW. Due to the Brownian motion of the CF-GNPs when immersed in the base fluid, every increase in the temperature of the produced nanofluids improved the thermal conductivity. At 50°C, the thermal conductivity increased by 31.6% for 0.1 wt.%. The linear relationship between mass concentration and improved thermal conductivity is due to the large expanses of particle-free liquid with high thermal resistance. Meanwhile, the relationship between an increase in thermal conductivity and a decrease in mass concentration is frequently nonlinear for nanoparticles with a high aspect ratio (such as MCNTs, nanorods, etc.) or nanoparticle alignment [51].

Figure 5(b) presents the effective dynamic viscosity of the base fluid and nanofluids at shear rate = 200 1/s and temperature in the range of 20-60°C. The dynamic viscosity of the CF-GNP nanofluids increased slightly due to the low CF-GNPs% in the DW. Although base fluids and nanofluids are both substantially temperature-dependent, it can also be shown in Figure 5(b) that viscosity reduced as temperature increased. This is predicted given the decrease of the adhesion forces between molecules and between particles, and practically all other types of nanofluids have shown comparable patterns. Low mass fractions were used to improve the

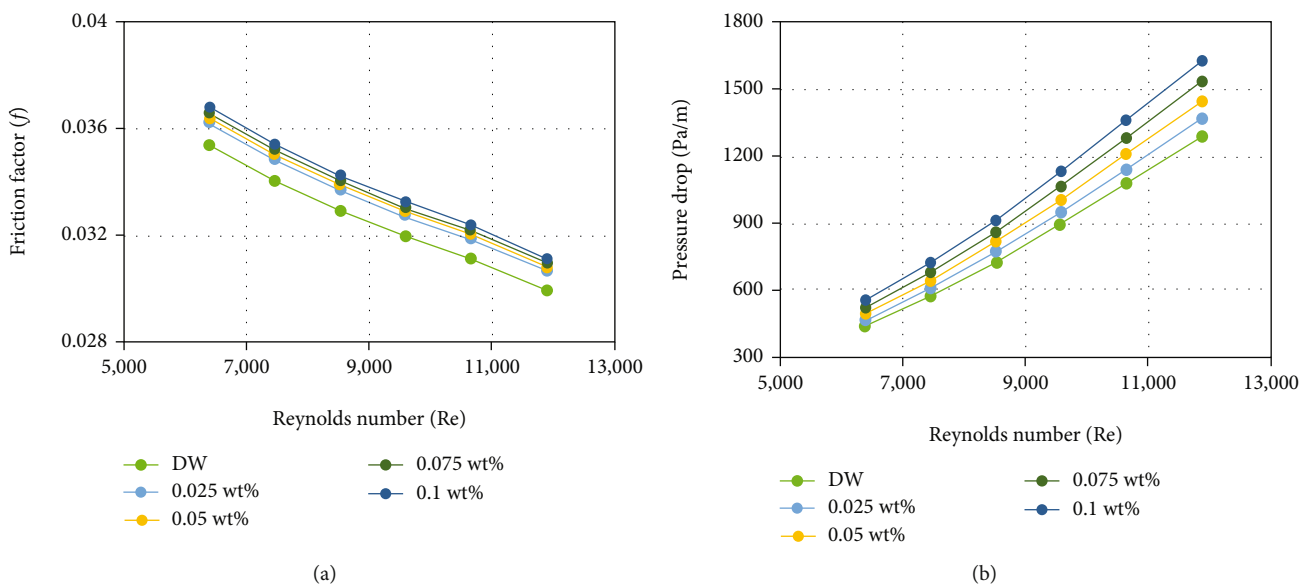

Figure 8: Fluid flow properties of CF-GNP nanofluids at various mass fractions versus Reynolds number: (a) friction factor; (b) pressure drop.

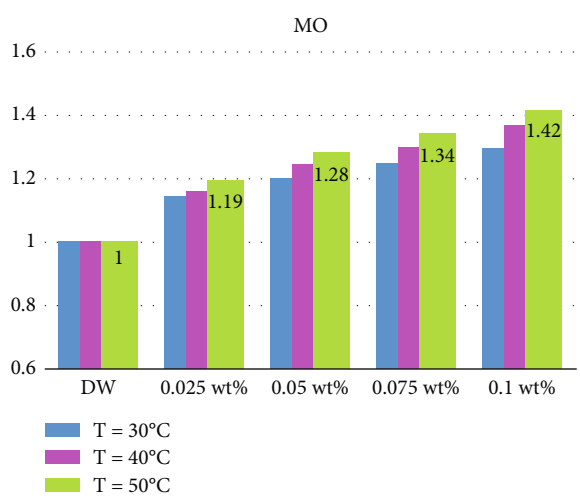

Figure 9: Mouromtseff criterion of base fluid and CF-GNPs nanofluids in different mass percentages at different inlet temperatures.

thermal conductivity of the nanofluids and minimize a dramatic increase in dynamic viscosity, which would necessitate more pumping power, which would be undesirable in real-world thermal applications. Also, the dynamic viscosity of CF-GNP nanofluids and DW decreased due to the loss of intermolecular forces [52, 53].

The density of CF-GNPs-DW nanofluids and DW were measured with a temperature range of 20-50°C (Figure 5(c)). A significant decrease in the density of the nanofluids as the temperature increased. Additionally, the density of CF-GNPs-DW nanosuspensions increased insignificantly with increases in the mass fraction. The reported rise in the density of CF-GNPs-DW was due to the higher density of solid NPs than that of the base fluid. A slight increase of 0.236% was observed in the density of the nanofluid at 0.1 wt.%-CF-GNPs and 20°C. Moreover, an increase in the fluid temperature from 20 to 50°C reduced the density by approximately 1.1%, demonstrating a critical role of temperature.

Figure 5(d) exhibited the collected data for specific heat capacity for base fluid and nanofluids. It was discovered that increasing the temperature of the sample did not influence the specific heat. These findings are consistent with prior publications' particular heat curves [54]. The addition of CF-GNP percentage in DW also resulted in a slight drop (0.88-1.38%) in the specific heat of the nano coolants. This was related to the fact that CF-GNPs had a lower specific heat than the base fluid.

3.2. Distilled Water as Working Fluid. Figures 6(a)–6(c) show the measured and collected data from Equations (1)–(3) heat transfer enhancement parameters (average Nusselt number and heat transfer coefficient). The results of heat transfer properties from the measurements and empirical correlations agreed well during the water run. The deviation between the experimental testing and the Petukhov equation was less than 8%. According to Cengel [55], the Gnielinski formula considers one of the most reliable comparisons for estimating the Nusselt number (Nu_{avg}) inside the heated pipe. Figures 6(b) and 6(d) depict the relative errors between the Nu number and average heat transfer coefficients between the experimental and theoretical parts during the water run. The values of Darcy friction factor during the water run were validated with two famous formulas of Blasius and Petukhov [56]. Blasius formula (see Equation (5)) can be considered the basic formula for estimating the Darcy friction factor due to its wide range of applications in the smooth heated pipes. The experimental and theoretical values of pressure loss and friction factor of the heated pipe were compared, as shown in Figures 6(e)–6(g). At the same

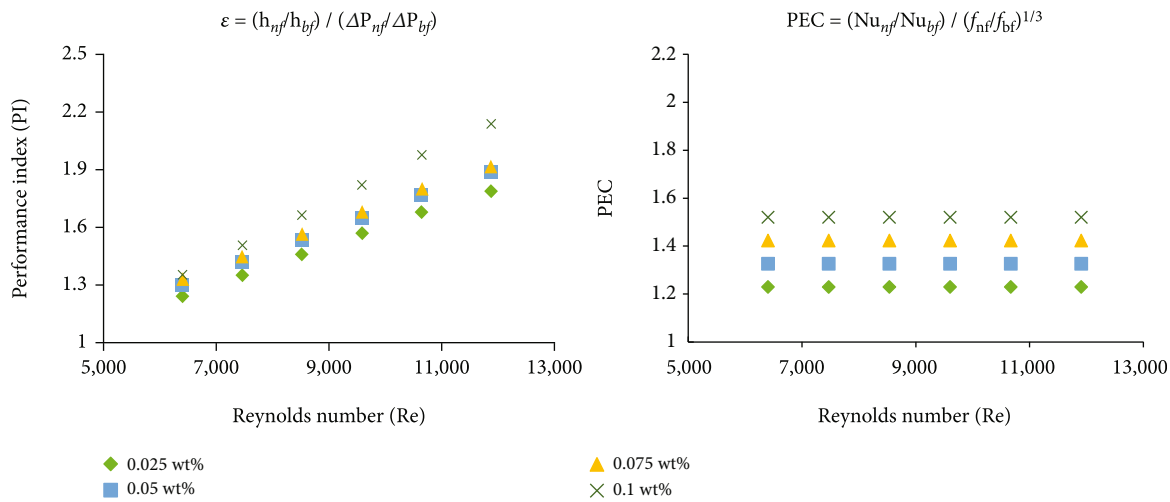

Figure 10: PI and PEC of CF-GNP nanofluids as a function of various mass fractions and versus Reynolds number.

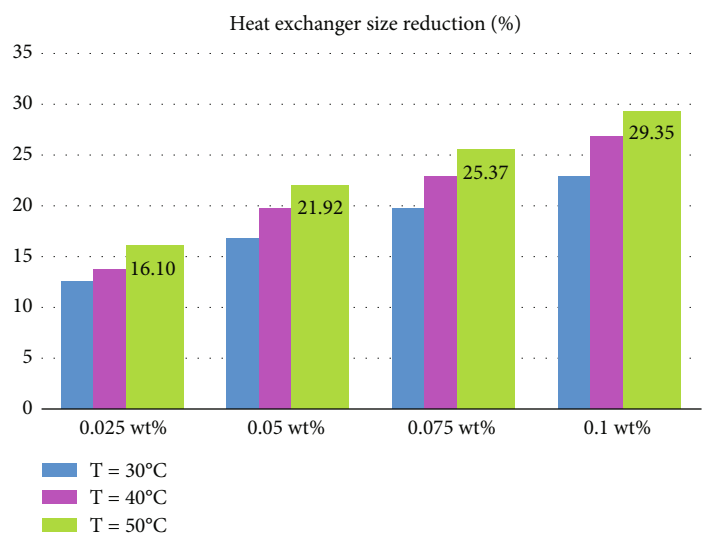

Figure 11: Heat exchanger size reduction of different mass percentages at different inlet temperatures.

time, Figures 6(f)–6(h) report the relative error between the measured and theoretical data for pressure drop and friction factor.

3.3. Heat Transfer Properties of CF-GNP Nanofluids. As earlier stated, the researchers avoid using surfactants in carbon-based nanofluid productions due to degradation at low-temperature [57], and they must be added in precise amounts. The ionic and nonionic polymers showed influences on hydrodynamic efficiency of colloidal nano-dispersion by trying to separate nanoparticles in the high mass fraction percentages. As per previous recommendations, the current nanomaterials were synthesized/prepared with no surfactant addition. The research aims to explain why manufactured nanofluids increase heat transport and fluid flow qualities in a heated square pipe.

Figure 7(a) presents heat transfer coefficients of the forced convective using CF-GNPs-DW nanofluids at different inlet flows (Reynolds numbers) with four samples. The heat transfer coefficient describes the convective heat transfer rate between the fluids' surface heated-wall and the working fluid medium. The mechanisms for improving heat transfer were the interactions between nanoparticles, chaotic particle motions, higher thermal energy transfer from the wall to the nanofluid flow, and the peculiarities of the dispersion properties. In addition, the process of improved heat transfer is significantly influenced by enhanced thermal conductivity and particle collisions [58, 59]. The current study revealed that using 0.1 wt.%-CF-GNPs-DW enhanced the heat transfer coefficient up to 44%, meanwhile using 0.025 wt.%-CF-GNPs-DW enhanced it to 33.3% at a constant heat flux of 11,205 W/m^2.

The Nusselt number (Nu) is the ratio between the convective rate and the developed nanomaterials' conductive rate as HTFs. Figure 7(b) shows the measuring values of the average Nu number as a function of Re number at

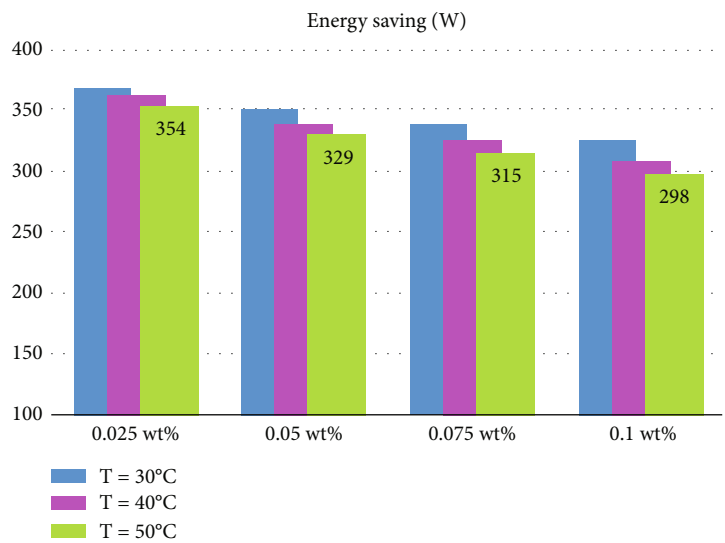

Figure 12: Energy savings for different mass percentages at different inlet temperatures.

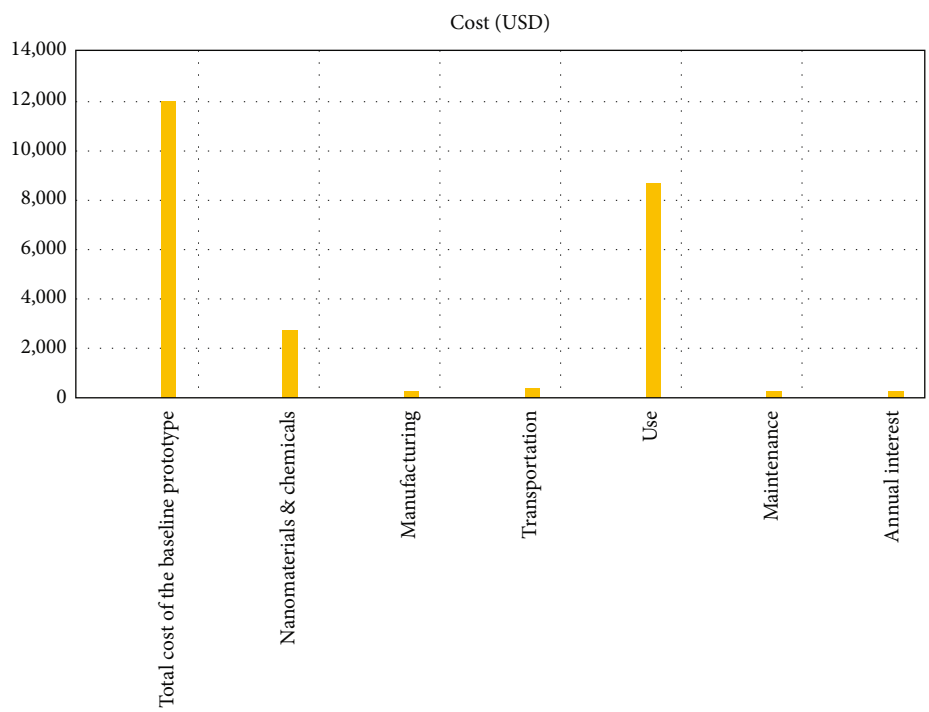

Figure 13: Total cost of the current thermal system running.

constant wall heat flux. The presented values of average Nu for CF-GNPs-DW nanofluids exhibited superb increases. The highest improvement in Nu was observed at 0.1 wt.%-CF-GNPs-H_2O, $q'' = 11{,}205\ W/m^2$, and $Re = 11{,}907$ with 35.1% relative to DW. The reported increase in Nu values resulted from the reduction in the circulation temperature due to the increase in the HTFs-thermal conductivity, which decreased the difference between the bulk fluid temperature and the surface heated-wall temperature.

3.4. Hydrodynamic Properties of CF-GNP Nanofluids. At various weight concentrations and Reynolds numbers, the friction factor and pressure loss values of the CF-GNP nanofluid were determined to be varied. Using four nanofluid samples, we measured the friction factor and pressure drop in Figures 8(a) and 8(b). In the meantime, despite the slight volatility in the examined data at various Re, Figure 8 revealed a minor increase with an increase in mass %. It was found that the largest pressure drop (20.8%) and friction factor (3.85%) were seen when the test circumstances were set to 0.1% CF-GNPs-H_2O and $v = 0.833$ m/s.

3.5. Economic and Thermal Analysis. Figure 9 shows the Mouromtseff criterion for different mass fractions and inlet

temperatures. On the other hand, the differences in the performance evaluation criterion (PEC) and performance index (PI) for various mass concentrations and Reynolds numbers are shown in Figure 10. All CF-GNP nanofluids had average PI and PEC values greater than 1, demonstrating the effectiveness of properly prepared nanofluids for effective heated-pipe flow utilization. Increases in CF-GNP weight concentration positively impacted the average PI and PEC compared to the pressure loss. Furthermore, increases in the Re and mass concentrations caused an increase in the PI of CF-GNPs-DW. For instance, at Re = 11,907 and $q'' = 11{,}205\ \mathrm{W/m^2}$, CF-GNPs-DW at a thermal efficiency of 0.1 wt.% showed the largest gain of 2.13. The PEC results also revealed a consistent decline in Re.

It is important to remember that fully developed flows can be accepted as cooling fluids in various cooling equipment owing to the turbulent flow nature of many fluids in most industrial and engineering applications, such as in heat exchangers. Again, an extensive study on nanofluid heat transfer coefficients demonstrates that they are even less effective than turbulent flow.

To better understand the performance of nanofluids in relation to their cost, the size reduction of heat exchangers is assessed using thermal efficiency values as shown in Figure 11. The heat exchanger size was reduced by 16.10%, 21.92%, 25.37%, and 29.35% for 0.025 wt.%, 0.05 wt.%, 0.075 wt.%, and 0.1 wt.%, respectively. In economics and engineering, using less size and more efficient heat exchangers than conventional base fluids will reduce the total production and manufacturing cost. Based on the reduced heat exchanger size, the energy savings are calculated and presented in Figure 12. The required power for base fluid was 422 W, then reduced to 354 W, 326 W, 315 W, and 298 W for 0.025 wt.%, 0.05 wt.%, 0.075 wt.%, and 0.1 wt.%, respectively. Furthermore, Figure 13 depicts the cost of manufacturing and production of the present thermal system, maintenance, and yearly interest. The total cost of the baseline prototype was USD 12020, nanomaterials and chemicals were USD 2765 (23% of the capital cost), manufacturing was USD 240 (2% of the capital cost), transportation was USD 361 (3% of the capital cost), system use was USD 8360 (72.3% of the capital cost), maintenance was USD 240 (2% of the capital cost), and annual interest was USD 240 (2% of the capital cost).

4. Conclusions

The nanomaterials of CF-GNPs were produced using a covalent functionalization approach as HTFs inside a square heated-pipe. The developed nanomaterials were characterized using different tools, and the thermal-physical were measured to achieve the study's current goal. Thermal and economic assessments were conducted to evaluate the current heat exchange system. The following conclusions were drawn from the study's findings:

(i) The functionalized graphene nanoplatelets (CF-GNPs) were characterized by different techniques such as zeta potential, particle size distributions, HR-TEM, SEM, and EDX to examine the stability and morphological properties

(ii) The prepared samples' thermophysical properties demonstrated significant operating performance in heated-pipe, with the most considerable improvement in thermal conductivity being 31.6% at 50°C and 0.1 wt.%.

(iii) The highest increments in the average Nusselt number and average heat transfer coefficient were 35.1% and 44.4%, respectively, using 0.1 wt.%-CF-GNPs-DW

(iv) The friction factor and nanofluid pressure loss increased by 3.85% and 20.8%, compared to the base fluid

(v) The prepared nanofluid showed PI, performance evaluation criterion, and Mouromtseff criteria of more than 1, which increased with the nanoparticles' higher mass content

(vi) The heat exchanger size reduced by 16.10%, 21.92%, 25.37%, and 29.35% for 0.025 wt.%, 0.05 wt.%, 0.075 wt.%, and 0.1 wt.%, respectively

(vii) The required power for base fluid was 422 W then reduced to 354 W, 326 W, 315 W, and 298 W for 0.025 wt.%, 0.05 wt.%, 0.075 wt.%, and 0.1 wt.%, respectively

(viii) The total cost of the baseline prototype was USD12020, nanomaterials and chemicals were USD 2765, manufacturing was USD 240, transportation was USD 361, system use was USD 8360, maintenance was USD 240, and annual interest was USD 240

Abbreviations

A_c:	Cross-section area (m^2)
Al_2O_3:	Aluminum oxide (alumina)
CF-GNPs:	Covalently functionalized graphene nanoplatelets
Cp:	Specific heat F (kJ/kg K)
CuO:	Copper oxide
D_h:	Hydraulic diameter (m)
DW:	Distilled water
DLS:	Dynamic light scattering
DSC:	Differential scanning calorimetry
EDX:	Energy-dispersive X-ray analysis
f:	Friction factor
FE-SEM:	Field emission scanning electron microscopy
FE-TEM:	Field emission transmission electron microscope
H_2SO_4:	Sulfuric acid
HNO_3:	Nitric acid
HTC:	Heat transfer coefficient
I:	Current (a)
KRG:	Alkaline oxide of graphene
LPM:	Liter per minute

$\dot{m}$: Mass flow rate (kg/s)
MO: Mouromtseff criterion
ΔP: Pressure loss (pa/m)
MWCNTs: Multiwalled carbon nanotube
MO: Mouromtseff of criteria
NIST: National Institute of Standards and Technology
Nu_{avg}: Average Nusselt number
P: Wetted perimeter
PEC: Performance evaluation criteria
PEG-TGr: Pentaethylene glycol-thermally treated graphene
P-GNPs: Pure graphene nanoplatelets
PI: Thermal performance index
Pr: Prandtl number
Pr_m: Prandtl number at bulk temperature
Pr_w: Prandtl number at wall temperature
PDI: Polydispersity index
Q: Power (watt)
Re: Reynolds number
RTD: Resistance temperature detectors
SiO_2: Silicon dioxide
SSA: Specific surface area
T_b: Bulk temperature (°C)
T_i: Inlet temperature (°C)
TiO_2: Titanium dioxide (titania)
T_o: Outlet temperature (°C)
T_w: Wall surface temperature (°C).

Data Availability

The data used for the current research is presented in the manuscript itself.

Disclosure

This research has been published as preprint, and reviewers/readers can refer to the following published version: https://assets.researchsquare.com/files/rs-1346926/v1_covered.pdf?c=1649681974, [60].

Conflicts of Interest

The authors declare no conflict of interest.

Acknowledgments

The authors would like to thank Al-Mustaqbal University College for providing technical support for this research. This research was carried out with the financial support of Al-Mustaqbal University College (MUC-E-0122).

References

[1] R. Vutukuru, A. S. Pegallapati, and R. Maddali, "Suitability of various heat transfer fluids for high temperature solar thermal systems," *Applied Thermal Engineering*, vol. 159, article 113973, 2019.

[2] O. A. Alawi, H. M. Kamar, A. R. Mallah et al., "Experimental and theoretical analysis of energy efficiency in a flat plate solar collector using monolayer graphene nanofluids," *Sustainability*, vol. 13, no. 10, p. 5416, 2021.

[3] O. A. Alawi, H. M. Kamar, O. A. Hussein et al., "Effects of binary hybrid nanofluid on heat transfer and fluid flow in a triangular-corrugated channel: an experimental and numerical study," *Powder Technology*, vol. 395, pp. 267–279, 2022.

[4] O. A. Alawi, A. H. Abdelrazek, M. S. Aldlemy et al., "Heat transfer and hydrodynamic properties using different metal-oxide nanostructures in horizontal concentric annular tube: An Optimization Study," *Nanomaterials*, vol. 11, no. 8, p. 1979, 2021.

[5] W. Ahmed, Z. Z. Chowdhury, S. N. Kazi et al., "Experimental evaluation and numerical verification of enhanced heat transportation by using ultrasonic assisted nanofluids in a closed horizontal circular passage," *Case Studies in Thermal Engineering*, vol. 26, article 101026, 2021.

[6] A. K. Hamzat, M. I. Omisanya, A. Z. Sahin, O. Ropo Oyetunji, and N. Abolade Olaitan, "Application of nanofluid in solar energy harvesting devices: a comprehensive review," *Energy Conversion and Management*, vol. 266, article 115790, 2022.

[7] H. Younes, M. Mao, S. M. Sohel Murshed, D. Lou, H. Hong, and G. P. Peterson, "Nanofluids: key parameters to enhance thermal conductivity and its applications," *Applied Thermal Engineering*, vol. 207, article 118202, 2022.

[8] W. Ajeeb and S. M. S. Murshed, "Nanofluids in compact heat exchangers for thermal applications: A State-of- the-art review," *Thermal Science and Engineering Progress*, vol. 30, article 101276, 2022.

[9] V. Srinivas, C. V. K. N. S. N. Moorthy, V. Dedeepya, P. V. Manikanta, and V. Satish, "Nanofluids with CNTs for automotive applications," *Heat and Mass Transfer*, vol. 52, no. 4, pp. 701–712, 2016.

[10] M. N. Pantzali, A. A. Mouza, and S. V. Paras, "Investigating the efficacy of nanofluids as coolants in plate heat exchangers (PHE)," *Chemical Engineering Science*, vol. 64, no. 14, pp. 3290–3300, 2009.

[11] S. A. Nada, R. M. el-Zoheiry, M. Elsharnoby, and O. S. Osman, "Enhancing the thermal performance of different flow configuration minichannel heat sink using Al_2O_3 and CuO- water nanofluids for electronic cooling: An experimental assessment," *International Journal of Thermal Sciences*, vol. 181, article 107767, 2022.

[12] Y.-P. Hu, F. J. Wang, Y. C. Zhang, Y. R. Li, and M. H. Li, "Oscillatory natural convection of Al_2O_3-water nanofluid near its density maximum in a narrow horizontal annulus," *International Communications in Heat and Mass Transfer*, vol. 136, article 106207, 2022.

[13] Y. Shang, R. Balali Dehkordi, S. Chupradit et al., "The computational study of microchannel thickness effects on H_2O/CuO nanofluid flow with molecular dynamics simulations," *Journal of Molecular Liquids*, vol. 345, article 118240, 2022.

[14] A. M. Ajeena, P. Víg, and I. Farkas, "A comprehensive analysis of nanofluids and their practical applications for flat plate solar collectors: fundamentals, thermophysical properties, stability, and difficulties," *Energy Reports*, vol. 8, pp. 4461–4490, 2022.

[15] A. Ghaffarkhah, A. Bazzi, Z. Azimi Dijvejin, M. Talebkeikhah, M. Keshavarz Moraveji, and F. Agin, "Experimental and numerical analysis of rheological characterization of hybrid nano-lubricants containing COOH-functionalized MWCNTs and oxide nanoparticles," *International Communications in Heat and Mass Transfer*, vol. 101, pp. 103–115, 2019.

[16] Z. Li, A. Kan, K. Wang, Y. He, N. Zheng, and W. Yu, "Optical properties and photothermal conversion performances of graphene based nanofluids," *Applied Thermal Engineering*, vol. 203, article 117948, 2022.

[17] M. Jamshidmofid and M. Bahiraei, "Thermohydraulic assessment of a novel hybrid nanofluid containing cobalt oxide-decorated reduced graphene oxide nanocomposite in a microchannel heat sink with sinusoidal cavities and rectangular ribs," *International Communications in Heat and Mass Transfer*, vol. 131, article 105769, 2022.

[18] A. Shibata, K. Fujimoto, and S. Torii, "Heat transfer enhancement of graphene nanofluid manufactured from graphite sheet," *Materials Today: Proceedings*, vol. 66, pp. 1852–1857, 2022.

[19] Z. Sun, S. Fang, and Y. H. Hu, "3D graphene materials: from understanding to design and synthesis control," *Chemical Reviews*, vol. 120, no. 18, pp. 10336–10453, 2020.

[20] Y. Wang, J. Mao, X. Meng, L. Yu, D. Deng, and X. Bao, "Catalysis with two-dimensional materials confining single atoms: concept, design, and applications," *Chemical Reviews*, vol. 119, no. 3, pp. 1806–1854, 2018.

[21] R. Banavath, S. S. Nemala, S. H. Kim et al., "Industrially scalable exfoliated graphene nanoplatelets by high-pressure airless spray technique for high-performance supercapacitors," *FlatChem*, vol. 33, article 100373, 2022.

[22] K. Dobrezberger, J. Bosters, N. Moser et al., "Hydrogenation on palladium nanoparticles supported by graphene nanoplatelets," *Journal of Physical Chemistry C*, vol. 124, no. 43, pp. 23674–23682, 2020.

[23] M. Sandhya, D. Ramasamy, K. Kadirgama, W. S. W. Harun, and R. Saidur, "Experimental study on properties of hybrid stable & surfactant-free nanofluids GNPs/CNCs (graphene nanoplatelets/cellulose nanocrystal) in water/ethylene glycol mixture for heat transfer application," *Journal of Molecular Liquids*, vol. 348, article 118019, 2022.

[24] J. I. Prado and L. Lugo, "Enhancing the thermal performance of a stearate phase change material with graphene nanoplatelets and MgO nanoparticles," *ACS Applied Materials & Interfaces*, vol. 12, no. 35, pp. 39108–39117, 2020.

[25] J. P. Vallejo, L. Mercatelli, M. R. Martina et al., "Comparative study of different functionalized graphene-nanoplatelet aqueous nanofluids for solar energy applications," *Renewable Energy*, vol. 141, pp. 791–801, 2019.

[26] L. H. Kumar, S. N. Kazi, H. H. Masjuki, M. N. M. Zubir, A. Jahan, and C. Bhinitha, "Energy, exergy and economic analysis of liquid flat-plate solar collector using green covalent functionalized graphene nanoplatelets," *Applied Thermal Engineering*, vol. 192, article 116916, 2021.

[27] M. Gosika, V. Velachi, M. N. D. S. Cordeiro, and P. K. Maiti, "Covalent functionalization of graphene with PAMAM dendrimer and its implications on graphene's dispersion and cytotoxicity," *ACS Applied Polymer Materials*, vol. 2, no. 8, pp. 3587–3600, 2020.

[28] S. S. Hamdi, H. H. al-Kayiem, A. S. Muhsan, and E. Magaril, "Experimental dataset on the dispersion stability of natural polymer non- covalently functionalized graphene nanoplatelets in high salinity brines," *Data in Brief*, vol. 31, p. 105702, 2020.

[29] S. S. Shazali, A. Amiri, M. N. Mohd Zubir et al., "Investigation of the thermophysical properties and stability performance of non-covalently functionalized graphene nanoplatelets with pluronic P-123 in different solvents," *Materials Chemistry and Physics*, vol. 206, pp. 94–102, 2018.

[30] M. Bahiraei and S. Heshmatian, "Graphene family nanofluids: a critical review and future research directions," *Energy Conversion and Management*, vol. 196, pp. 1222–1256, 2019.

[31] R. Sadri, M. Hosseini, S. N. Kazi et al., "A facile, bio-based, novel approach for synthesis of covalently functionalized graphene nanoplatelet nano-coolants toward improved thermophysical and heat transfer properties," *Journal of Colloid and Interface Science*, vol. 509, pp. 140–152, 2018.

[32] S. S. Shazali, S. Rozali, A. Amiri, M. N. M. Zubir, M. F. M. Sabri, and M. Z. Zabri, "Evaluation on stability and thermophysical performances of covalently functionalized graphene nanoplatelets with xylitol and citric acid," *Materials Chemistry and Physics*, vol. 212, pp. 363–371, 2018.

[33] Y. Wang, H. A. I. al-Saaidi, M. Kong, and J. L. Alvarado, "Thermophysical performance of graphene based aqueous nanofluids," *International Journal of Heat and Mass Transfer*, vol. 119, pp. 408–417, 2018.

[34] O. A. Alawi, A. R. Mallah, and S. N. Kazi, "Covalently functionalized pentaethylene glycol-thermally treated graphene towards enhanced thermophysical and heat transfer characteristics," *Journal of Thermal Analysis and Calorimetry*, vol. 140, no. 2, pp. 859–874, 2020.

[35] A. H. Abdelrazek, S. N. Kazi, O. A. Alawi, N. Yusoff, C. S. Oon, and H. M. Ali, "Heat transfer and pressure drop investigation through pipe with different shapes using different types of nanofluids," *Journal of Thermal Analysis and Calorimetry*, vol. 139, no. 3, pp. 1637–1653, 2020.

[36] E. Montazer, M. B. Shafii, E. Salami et al., "Heat transfer in turbulent nanofluids: separation flow studies and development of novel correlations," *Advanced Powder Technology*, vol. 31, no. 8, pp. 3120–3133, 2020.

[37] S. Dayou, T. W. Ting, and B. Vigolo, "Comparison of heat transfer performance of water-based graphene nanoplatelet- and multi-walled carbon nanotube-nanofluids in a concentric tube heat exchanger," *Diamond and Related Materials*, vol. 125, article 108976, 2022.

[38] O. A. Hussein, K. Habib, R. Saidur, A. S. Muhsan, S. Shahabuddin, and O. A. Alawi, "The influence of covalent and non-covalent functionalization of GNP based nanofluids on its thermophysical, rheological and suspension stability properties," *RSC Advances*, vol. 9, no. 66, pp. 38576–38589, 2019.

[39] J. Buongiorno, D. C. Venerus, N. Prabhat et al., "A benchmark study on the thermal conductivity of nanofluids," *Journal of Applied Physics*, vol. 106, no. 9, p. 094312, 2009.

[40] J. Fernandez-Seara, F. J. Uhía, J. Sieres, and A. Campo, "A general review of the Wilson plot method and its modifications to determine convection coefficients in heat exchange devices," *Applied Thermal Engineering*, vol. 27, no. 17–18, pp. 2745–2757, 2007.

[41] B. S. Petukhov, "Heat transfer and friction in turbulent pipe flow with variable physical properties," *Advances in Heat Transfer*, vol. 6, pp. 503–564, 1970.

[42] V. Gnielinski, "New equations for heat and mass transfer in the turbulent flow in pipes and channels," *NASA STI/recon Technical Report A*, vol. 75, pp. 8–16, 1975.

[43] C. F. Colebrook, "Turbulent flow in pipes, with particular reference to the transition region between the smooth and rough pipe laws," *Journal of the Institution of Civil Engineers*, vol. 11, no. 4, pp. 133–156, 1939.

[44] E. Sadeghinezhad, M. Mehrali, S. Tahan Latibari et al., "Experimental investigation of convective heat transfer using graphene nanoplatelet based nanofluids under turbulent flow conditions," *Industrial and Engineering Chemistry Research*, vol. 53, no. 31, pp. 12455–12465, 2014.

[45] H. Blasius, "Grenzschichten in Flussigkeiten mit kleiner Reibung," *Druck von BG Teubner*, 1907.

[46] S. K. Das, N. Putra, P. Thiesen, and W. Roetzel, "Temperature dependence of thermal conductivity enhancement for nanofluids," *Journal of Heat Transfer*, vol. 125, no. 4, pp. 567–574, 2003.

[47] E. V. Timofeeva, J. L. Routbort, and D. Singh, "Particle shape effects on thermophysical properties of alumina nanofluids," *Journal of Applied Physics*, vol. 106, no. 1, article 014304, 2009.

[48] W. Yu, D. M. France, E. V. Timofeeva, D. Singh, and J. L. Routbort, "Comparative review of turbulent heat transfer of nanofluids," *International journal of heat and mass transfer*, vol. 55, no. 21, pp. 5380–5396, 2012.

[49] Z. Xuan, Y. Zhai, M. Ma, Y. Li, and H. Wang, "Thermo-economic performance and sensitivity analysis of ternary hybrid nanofluids," *Journal of Molecular Liquids*, vol. 323, article 114889, 2021.

[50] M. L. V. Ramires, C. A. Nieto de Castro, Y. Nagasaka, A. Nagashima, M. J. Assael, and W. A. Wakeham, "Standard reference data for the thermal conductivity of water," *Journal of Physical and Chemical Reference Data*, vol. 24, no. 3, pp. 1377–1381, 1995.

[51] M. Chandrasekar, S. Suresh, and A. Chandra Bose, "Experimental investigations and theoretical determination of thermal conductivity and viscosity of Al2O3/water nanofluid," *Experimental Thermal and Fluid Science*, vol. 34, no. 2, pp. 210–216, 2010.

[52] S. S. J. Aravind, P. Baskar, T. T. Baby, R. K. Sabareesh, S. Das, and S. Ramaprabhu, "Investigation of structural stability, dispersion, viscosity, and conductive heat transfer properties of functionalized carbon nanotube based nanofluids," *Journal of Physical Chemistry C*, vol. 115, no. 34, pp. 16737–16744, 2011.

[53] M. M. M. Mehrali, E. Sadeghinezhad, S. T. Latibari et al., "Investigation of thermal conductivity and rheological properties of nanofluids containing graphene nanoplatelets," *Nanoscale Research Letters*, vol. 9, no. 1, p. 15, 2014.

[54] B. C. Pak and Y. I. Cho, "Hydrodynamic and heat transfer study of dispersed fluids with submicron metallic oxide particles," *Experimental Heat Transfer*, vol. 11, no. 2, pp. 151–170, 1998.

[55] Y. A. Cengel, *Heat transfer: a practical approach*, McGraw-Hill, New York, 2003.

[56] S. N. Kazi, G. G. Duffy, and X. D. Chen, "Validation of heat transfer and friction loss data for fibre suspensions in a circular and a coaxial pipe heat exchanger," *International Journal of Thermal Sciences*, vol. 79, pp. 146–160, 2014.

[57] M. U. Sajid and H. M. Ali, "Recent advances in application of nanofluids in heat transfer devices: a critical review," *Renewable and Sustainable Energy Reviews*, vol. 103, pp. 556–592, 2019.

[58] B. Kristiawan, A. T. Wijayanta, K. Enoki, T. Miyazaki, and M. Aziz, "Heat transfer enhancement of TiO_2/water nanofluids flowing inside a square minichannel with a microfin structure: a numerical investigation," *Energies*, vol. 12, no. 16, p. 3041, 2019.

[59] S. Liu, H. A. Afan, M. S. Aldlemy, N. al-Ansari, and Z. M. Yaseen, "Energy analysis using carbon and metallic oxides-based nanomaterials inside a solar collector," *Energy Reports*, vol. 6, pp. 1373–1381, 2020.

[60] R. S. Mohammad, M. S. Aldlemy, M. W. Falah, R. Z. Homod, and Z. M. Yaseen, *Thermal analysis of graphene based nanofluids for energy system and economic feasibility*, Researchsquare, 2022.

Hindawi
Journal of Nanomaterials
Volume 2022, Article ID 1915185, 15 pages
https://doi.org/10.1155/2022/1915185

Research Article

Entropy Analysis in Bidirectional Hybrid Nanofluid Containing Nanospheres with Variable Thermal Activity

Iftikhar Ahmad,[1] Qazi Zan-Ul-Abadin,[1] Muhammad Faisal,[1] K. Loganathan,[2,3] Tariq Javed,[4] and Sonam Gyeltshen[5]

[1]*Department of Mathematics, Azad Jammu & Kashmir University, Muzaffarabad 13100, Pakistan*
[2]*Research and Development Wing, Live4Research, Tiruppur, 638106 Tamil Nadu, India*
[3]*Department of Mathematics and Statistics, Manipal University Jaipur, Jaipur, 303007 Rajasthan, India*
[4]*Department of Mathematics and Statistics, International Islamic University, Islamabad 44000, Pakistan*
[5]*Department of Humanities and Management, Jigme Namgyel Engineering College, Royal University of Bhutan, Dewathang, Bhutan*

Correspondence should be addressed to Muhammad Faisal; muhamamd.faisal@ajku.edu.pk, K. Loganathan; loganathankaruppusamy304@gmail.com, and Sonam Gyeltshen; sonamgyeltshen@jnec.edu.bt

Received 19 May 2022; Revised 18 June 2022; Accepted 5 July 2022; Published 18 July 2022

Academic Editor: Hafiz Muhammad Ali

An investigation of the thermal performance of water-conveying nanospheres (magnetite (Fe_3O_4) and silver (Ag)) subject to variable thermal controls, namely, variable surface temperature and variable surface normal heat flux, has been made. A bidirectionally elongating surface is used to generate an unsteady flow mechanism with the action of the Lorentz force. Derived equations of basic laws are firstly nondimensionalized and then numerically solved by applying the Keller-Box method. The local Nusselt number for both the thermal cases is calculated and discussed. Percent-wise enhancement in the rate of heat transport has also been included in the analysis. It was concluded through the present exploration that at lower volume fractions of magnetite and silver, the rate of heat transport is observed to be dominant. The rate of heat transference has attained identical values for both the provided thermal conditions at the surface. Moreover, intensities of velocity and thermal profiles diminish with the appreciation of the choice of unsteadiness. The temperature-controlling indices also affect the thermal profile, and it is reduced with the intensification in the considerations of these indices. The values of thermal conductivity, density, and electrical conductivity have been improved with the inclusion of nanospheres (magnetite (Fe_3O_4) and silver (Ag)), whereas the value of specific heat is reduced with the mixture of these nanospheres. The Nusselt number is increased up to 5% with the involvement of magnetite nanospheres, and it is enhanced up to 4% with the involvement of silver nanospheres.

1. Introduction

A staggering and unprecedented advancement in the field of microelectronics, microfluidics, chemical synthesis, optical devices, high-power engines, shipping, microsystems, and electrical and mechanical components has entirely transformed the foundations of human life. These developments additionally demand effective cooling procedures in order to explore the performance of thermal conductivity and reliability of operational devices. The basic idea of controlling the thermal efficiency via cooling through fluids seems to be deficient, and hence, this issue has been resolved by submerging the tiny particles into the host fluid that certainly affects its thermomechanical possessions. This colloidal mixture of tiny particles into the host fluid is famous for the name nanofluid. Famous theoretical models regarding the study of thermal conductivity have been proposed by Choi et al. [1], Maxwell [2], and Bruggeman [3]. The pioneer nanofluid model for the study of tiny particle shapes/sizes is presented by Hamilton and Crosser [4], and it shows that the shapes of the dispersed tiny particles sufficiently affect the thermophysical behavior of heterogeneous substances.

Later on, Masoumi et al. [5] presented the model to compute the operative viscosity of nanomaterials. The development of knowledge in the field of nanofluid has also led us to the understanding of tiny particle shapes/sizes as an important factor causing changes in thermal conductivity and viscosity. Some more recent developments in the existing nanofluid models regarding the shapes/sizes of nanoparticles are disclosed by Mooney [6] and Ohshima [7]. In these nanofluid models, it is inferred that the thermal conductivity performance of water-conveying nanomaterial is significantly improved by submerging the nanospheres. Some more extraordinary explorations regarding the control of the nanoparticle shape factor on the thermal executions of various substances are made by the researchers via Refs. [8–12].

Recently, an improved class of nanofluids with the name hybrid nanofluid has come into existence to bear the high performance of thermal conductivity associated with the mono-nanofluid. With the utilization of hybrid nanofluids, revolutionary applications in the field of heat transfer processes are found in generator and nuclear cooling systems, automobile radiators, electronic cooling with coolants in the machinery, solar heating, welding, lubrication, drug reduction, biomedicine, cooling and heating in buildings, and defense. The main issue for the regular nanofluid network is that they either have a good thermal conductive performance or have a better rheological setup. Single-handedly, they do not possess all the necessary properties which are mandatory for a certain heat exchanger application. Therefore, with the suitable choice of two or more nanoparticles, hybrid nanofluid can provide us with a well-suited mixture, which owns all physicochemical features of different substances that can scarcely be found in a separate substance. These distinctive properties of hybrid nanofluids have increased the attention of worldwide investigators, and therefore, many research articles have been published in this fascinating field over the last decade. Numerical exploration regarding the 3D flow of hybrid nanofluid $(Cu - Al_2O_3/H_2O)$ towards an expanding obstacle with the significance of the Newtonian heating and Lorentz force is made by Devi and Devi [13] and obtained that the frequency of heat transference for the hybrid nanofluid is much better than that for the ordinary nanofluid even with the effect of the magnetic environment. Hayat et al. [14] conferred the 3D radiative dynamics of hybrid nanofluid $(Ag - CuO/H_2O)$ impinging over a bidirectionally expanding slippery surface in a rotating frame and concluded that the rate of heat transference of the hybrid nanofluid is improved as compared to that of the traditional nanofluid. The detailed analysis of the thermal conductivity and viscosity of hybrid nanofluid $(Al_2O_3 - CuO)$ with ethylene glycol and propylene glycol binary host fluid with different shapes of nanoparticles (i.e., spherical, cylindrical, platelet, blade, and brick) is disclosed by Kumar and Sahoo [15] and concluded that the nanoparticles having spherical shapes have two percent higher thermal conductivity to that of platelet-shaped nanoparticles. Moreover, the impact of volume fraction on nanoparticles is detected incredibly in the thermal conductivity of nanofluids. Nabil et al. [16] comprehensively discussed the thermophysical features of hybrid nanofluids and hybrid nanolubricants with potential applications in the engineering sector with the predictions of their future utilization. Rashid and Liang [17] presented the numerical solution for the dynamics of MHD nanofluid with the significance of different shapes of nanoparticles over a rotating stretchable obstacle through a porous domain. A theoretical investigation regarding the transitory steady flow of water-conveying hybrid nanofluid containing magnetite and silver nanospheres is conducted by Nabwey and Mahdy [18]. Zainal et al. [19] numerically explored the impact of MHD on the steady bidirectional flow of hybrid nanofluid containing copper and aluminum oxide nanoparticles with water as host fluid. Besides, many researchers [20–25] have contributed to the field of hybrid nanofluid with various thermal engineering aspects.

Passive/variable thermal aspects play a significant role in the development of aircraft cooling frames, heat exchanger devices, fuselage condensation processes, air conditioning condensers, refrigeration systems, electric heaters, power converters, motor controllers, and many other industrial and mechanical applications. Oliveira et al. [26] presented a design for a passive heat exchanger system to control the cooling system of aircraft for variable thermal conditions. In this investigation, water is considered a host liquid with the features of natural, forced, and mixed convection. The aspects of passive heating on the dynamics of fluid in the boundary layer zone are initially discussed by Liu and Andersson [27] by considering the variable surface temperature (VST) and variable surface heat flux (VHF) mechanisms. The rate of heat transference is expressively enhanced with the presence of these heating mechanisms. Ahmad et al. [28] numerically disclosed the unsteady 3D flow of copper-water nanofluid with variable thermal aspects. Ahmad et al. [29] also reported the unsteady 3D rotating flow of nanofluid with the aspects of the prescribed thermal environment. The hybrid nanofluid flow over an expanding cylinder with the characteristic of prescribed surface heat flux is examined by Waini et al. [30]. Waini et al. [31] also disclosed the significance of prescribed surface heat flux on the dynamics of hybrid nanofluid past over a thin needle. Khashi'ie et al. [32] discussed the flow of hybrid nanofluid over a shrinking domain with prescribed thermal conditions. The effect of suspended particles on the flow of nanofluid with the effect of VST and VHF mechanisms is also analyzed by Gireesha et al. [33]. Some leading explorations regarding the outcomes of prescribed thermal conditions on the flow of nanofluids as well as hybrid nanofluids are found via Refs. [34–37].

Entropy is a physical property of the system that obeys the thermodynamic second law. It measures the level of disorderliness and unproductive energy within the environment. The entropy of a reversible system is constant, whereas the entropy of an irreversible system varies with the factors involved in transport equations. In general, real processes are reversible (i.e., the system responds according

to the environmental scenario). Entropy transport in hybrid nanofluid is a new area of research and got considerable importance nowadays. Entropy transport in nanofluids as well as hybrid nanofluids within the thermal environment is inquired by Huminic and Huminic [38]. Khan et al. [39] scrutinized the entropy transport in the rotatory flow of hybrid nanofluid influenced by magnetization. Heat transport and entropy transport in hybrid nanofluids packed in a flattened tube are examined by Huminic and Huminic [40]. Entropy transport with temperature-controlled viscosity in hybrid nanofluid comprising single-walled as well as multiwalled carbon nanotubes is elaborated by Ahmad et al. [41]. Entropy transport in the peristaltic-type flow of hybrid nanofluid is reported by Zahid et al. [42]. Hussien et al. [43] discussed the entropy and thermal transport in hybrid nanofluids by considering microtubes. Sheikholeslami et al. [44] considered the entropy transport in hybrid nanofluid contained in a porous tank with the impact of the Lorentz force. Heat and entropy transport assessment in the bidirectional flow of hybrid nanofluid by the movement of convectively heating devices is disclosed by Upreti et al. [45]. Saleh and Sundar [46] focused on entropy and exergy transport in hybrid nanofluid containing nanodiamond in a circular tube. Recently, Eswaramoorthi et al. [47] investigated the entropy and heat transport in magnetized water-driven nanofluid over a bidirectional moving device with a radiation phenomenon.

The above literature survey reveals the statement that no attention has been given in order to investigate the unsteady 3D entropy optimized flow of water-based hybrid nanofluid containing nanospheres, i.e., magnetite and silver, towards an elongating surface with passive thermal controls. The effect of the Lorentz force is also considered in the modeling for physical relevancy. A passive heat controlling system consists of both variable surface temperature and variable surface heat flux mechanisms. Similarity transformations have been used to accomplish the mathematical model for solvable situations. The Keller-Box method [48–52] with Newton's linearization scheme has been endorsed to find the numerical solution of the modeled problem. The validity of the acquired results is discussed through the grid-independent tactic. The graphical aids have been provided to discuss the influence of various emerging entities on thermal as well as entropy setups. The relations based on the coefficient of skin friction, entropy formation, Bejan number, and local Nusslet number have also been derived and discussed through various scientific patterns.

2. Mathematical Formulation

The mathematical formulation of the problem has been completed in view of the undermentioned assumptions:

(i) Incompressible, laminar, and unsteady flow

(ii) Bidirectional stretching

(iii) Thermal equilibrium situation of nanospheres (i.e., magnetite and silver) with water

(iv) No-slip condition at the surface within the boundary layer region

(v) Utilization of variable thermal conditions

(vi) Magnetohydrodynamic three-dimensional flow

(vii) Entropy and heat transport

2.1. Flow Description. The Cartesian configuration is used to frame an unsteady mathematical model regarding the dynamics of hybrid nanofluid containing nanospheres (Fe_3O_4 and Ag) suspended in water towards a bidirectionally elongating surface. Magnetite nanospheres can be used in the process of water purification, drug delivery, and steel manufacturing, whereas silver is the best electrical as well as thermal conductor among all metals and hence ideal for electrical applications. The concept of variable magnetic field $B(t) = B_0/\sqrt{1-ct}$ having strength B_0 is externally applied through the Lorentz force in the absence of an electric field. The nanospheres are in thermal equilibrium with the base liquid. The concept of the no-slip condition at the surface within the boundary stream is also utilized for laminar and incompressible flow. The hybrid nanofluid is restricted in the domain $0 < z < \infty$, whereas the disturbance in the hybrid nanofluid is created through expansion velocity $u_w = ax/(1-ct)(a > 0, c > 0)$ along the x-direction and expansion velocity $v_w = by/(1-ct)(b \geq 0)$ along the y-direction of the system configuration (as shown in Figure 1). The thermophysical properties of water H_2O, magnetite Fe_3O_4, and silver Ag are included in the mathematical modeling through Table 1.

In view of the aforementioned assumptions, component forms of governing equations are composed as (Ref. [12])

$$\frac{\partial u}{\partial x} + \frac{\partial v}{\partial y} + \frac{\partial w}{\partial z} = 0, \tag{1}$$

$$\frac{\partial u}{\partial t} + u\frac{\partial u}{\partial x} + v\frac{\partial u}{\partial y} + w\frac{\partial u}{\partial z} = \frac{\mu_{\text{hnf}}}{\rho_{\text{hnf}}}\frac{\partial^2 u}{\partial z^2} - \frac{\sigma_{\text{hnf}}}{\rho_{\text{hnf}}}B(t)^2 u, \tag{2}$$

$$\frac{\partial v}{\partial t} + u\frac{\partial v}{\partial x} + v\frac{\partial v}{\partial y} + w\frac{\partial v}{\partial z} = \frac{\mu_{\text{hnf}}}{\rho_{\text{hnf}}}\frac{\partial^2 v}{\partial z^2} - \frac{\sigma_{\text{hnf}}}{\rho_{\text{hnf}}}B(t)^2 v, \tag{3}$$

with (Ref. [9])

$$\begin{aligned}
\rho_{\text{hnf}} &= \psi_1\rho_{p1} + \psi_2\rho_{p2} + (1-\psi_1-\psi_2)\rho_{\text{f}},\\
\frac{\sigma_{\text{hnf}}}{\sigma_{\text{bf}}} &= 1 + \frac{3\left(\left(\sigma_{p2}/\sigma_{\text{bf}}\right)-1\right)\psi_2}{\left(\sigma_{p2}/\sigma_{\text{bf}}\right)+2-\left(\left(\sigma_{p2}/\sigma_{\text{bf}}\right)-1\right)\psi_2},\\
\frac{\sigma_{\text{bf}}}{\sigma_{\text{f}}} &= 1 + \frac{3\left(\left(\sigma_{p1}/\sigma_{\text{f}}\right)-1\right)\psi_1}{\left(\sigma_{p1}/\sigma_{\text{f}}\right)+2-\left(\left(\sigma_{p1}/\sigma_{\text{f}}\right)-1\right)\psi_1},\\
\frac{\mu_{\text{hnf}}}{\mu_{\text{bf}}} &= 1 + 2.5\psi_2 + 6.2{\psi_2}^2,\\
\frac{\mu_{\text{bf}}}{\mu_{\text{f}}} &= 1 + 2.5\psi_1 + 6.2{\psi_1}^2.
\end{aligned} \tag{4}$$

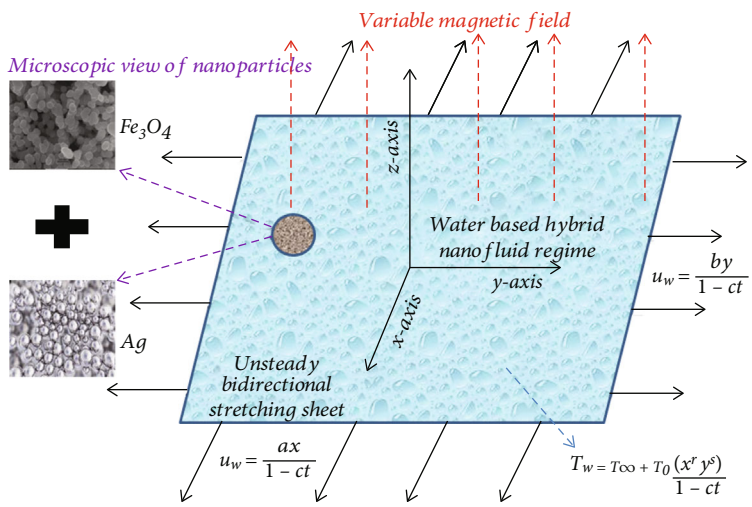

Figure 1: Graphical abstract of the mathematical model.

Table 1: Thermophysical features of water, magnetite nanoparticles, and silver nanoparticles (Ref. [20]).

Thermophysical features	Base fluid H_2O	Nanoparticles $Fe_3O_4(\psi_1)$	$Ag(\psi_2)$
Density: ρ (kgm^{-3})	997.1	5180	10500
Thermal conductivity: k ($Wm^{-1}K^{-1}$)	0.613	9.7	429
Specific heat: C_p ($Jkg^{-1}K^{-1}$)	4179	670	235
Electrical conductivity: σ ($\Omega^{-1}m^{-1}$)	0.05	2.5×10^4	6.3×10^7
Prandtl number: Pr	6.20	—	—

Supported BCs are (Ref. [34])

$$z = 0 : u = u_w(x,t) = \frac{ax}{1-ct}, v = v_w(y,t) = \frac{by}{1-ct}, w = 0, \tag{5}$$

$$z \longrightarrow \infty : u \longrightarrow 0, v \longrightarrow 0. \tag{6}$$

Similarity variables comprise (Ref. [35])

$$u = \frac{ax}{1-ct} f'(\eta), \tag{7}$$

$$v = \frac{ay}{1-ct} g'(\eta), \tag{8}$$

$$w = -\left(\frac{a\vartheta_f}{1-ct}\right)^{1/2} [f(\eta) + g(\eta)], \tag{9}$$

$$\eta = \left(\frac{a}{\vartheta_f(1-ct)}\right)^{1/2} z. \tag{10}$$

In the application of equation (7), equation (1) is identically balanced and equations (2)–(5) are of the following forms:

$$\varepsilon_1 f''' - f'^2 + (f+g)f'' - S\left(f' + \frac{\eta}{2} f''\right) - \varepsilon_2 M^2 f' = 0,$$
$$\varepsilon_1 g''' - g'^2 + (f+g)g'' - S\left(g' + \frac{\eta}{2} g''\right) - \varepsilon_2 M^2 g' = 0, \tag{11}$$

with

$$f(0) + g(0) = 0, \tag{12}$$

$$f'(0) = 1, \tag{13}$$

$$g'(0) = \alpha, \tag{14}$$

$$f'(\infty) \longrightarrow 0, \tag{15}$$

$$g'(\infty) \longrightarrow 0. \tag{16}$$

In the bidirectional flow, authors are generally concentrating on choosing the range of α as $0 < \alpha < 1$ because for $\alpha > 1$, the axes x and y are interchanged, and for $\alpha = 1$, the stretching rate becomes alike in both directions; thus, the flow profile turns out to be axisymmetric. Also, considering the limiting situation (i.e., $\alpha \longrightarrow 0$), the flow becomes unidirectional. Wang [53] reported that without any loss of generality, the condition $f(0) + g(0) = 0$ can be restored by $f(0) = 0$ and $g(0) = 0$. Further, in equations (1)–(12), velocity measures corresponding to the (x, y, z)-directions are (u, v, w), respectively. The presence

of time is denoted by t, whereas the temperature is symbolized by T, and hnf stands for the hybrid nanofluid, bf symbolizes the base fluid, nf discusses the nanofluid, μ expresses the viscosity, ρ reports the density, σ evokes the electrical conductivity, p_1 depicts the magnetite nanoparticles having concentration ψ_1, p_2 illustrates the silver nanoparticles having concentration ψ_2, and (f, g, η) posts the similarity variables with the involvement of ϑ_f (i.e., kinematic viscosity). Moreover, $S = c/a$, $M = (\sigma_f/a\rho_f)^{1/2}B_0$, and $\alpha = b/a$ diagnose the unsteady, magnetic, and expansion ratio parameters, respectively. The coefficients ε_1 and ε_2 are communicated as (Refs. [9, 12])

$$\varepsilon_1 = \frac{\left(1 + 2.5\psi_2 + 6.2{\psi_2}^2\right)\left(1 + 2.5\psi_1 + 6.2{\psi_1}^2\right)}{\left(\psi_1\left(\rho_{p1}/\rho_f\right) + \psi_2\left(\rho_{p2}/\rho_f\right) + (1 - \psi_1 - \psi_2)\right)},$$
$$\varepsilon_2 = \frac{\left(1 + \left(3\left(\left(\sigma_{p2}/\sigma_{bf}\right) - 1\right)\psi_2/\left(\left(\sigma_{p2}/\sigma_{bf}\right) + 2 - \left(\left(\sigma_{p2}/\sigma_{bf}\right) - 1\right)\psi_2\right)\right)\right)\left(1 + \left(3\left(\left(\sigma_{p1}/\sigma_f\right) - 1\right)\psi_1/\left(\left(\sigma_{p1}/\sigma_f\right) + 2 - \left(\left(\sigma_{p1}/\sigma_f\right) - 1\right)\psi_1\right)\right)\right)}{\psi_1\left(\rho_{p1}/\rho_f\right) + \psi_2\left(\rho_{p2}/\rho_f\right) + (1 - \psi_1 - \psi_2)}. \tag{17}$$

2.2. Heat Transport. In the current model, the heat transport phenomenon can be described by the following equation:

$$\frac{\partial T}{\partial t} + u\frac{\partial T}{\partial x} + v\frac{\partial T}{\partial y} + w\frac{\partial T}{\partial z} = \frac{k_{hnf}}{\left(\rho C_p\right)_{hnf}}\frac{\partial^2 T}{\partial z^2}, \tag{18}$$

with (Ref. [9])

$$\left(\rho C_p\right)_{hnf} = \psi_1\left(\rho C_p\right)_{p1} + \psi_2\left(\rho C_p\right)_{p2} + (1 - \psi_1 - \psi_2)\left(\rho C_p\right)_f,$$
$$\frac{k_{hnf}}{k_{bf}} = \frac{\left(k_{p2} + 2k_{bf}\right) + 2\psi_2\left(k_{p2} - k_{bf}\right)}{\left(k_{p2} + 2k_{bf}\right) - \psi_2\left(k_{p2} - k_{bf}\right)},$$
$$\frac{k_{bf}}{k_f} = \frac{\left(k_{p1} + 2k_f\right) + 2\psi_1\left(k_{p1} - k_f\right)}{\left(k_{p1} + 2k_f\right) - \psi_1\left(k_{p1} - k_f\right)}. \tag{19}$$

Here, two types of thermal BCs are used to discuss the variable thermal activity. These are variable surface temperature (VST) and variable surface heat flux (VHF). Mathematically, we have

$$\text{VST case}: z = 0: T = T_w(x, y, t) = T_\infty + T_0\left(\frac{x^r y^s}{1 - ct}\right), z \longrightarrow \infty: T \longrightarrow T_\infty,$$
$$\text{VHF case}: z = 0: -k_f\left(\frac{\partial T}{\partial z}\right)_w = q_w(x, y, t) = T_1\left(\frac{x^r y^s}{1 - ct}\right), z \longrightarrow \infty: T \longrightarrow T_\infty. \tag{20}$$

Similarity transformations for both the thermal activities are (Ref. [12])

$$\text{VST case}: \theta(\eta) = \frac{T(x, y, z, t) - T_\infty}{T_w(x, y, t) - T_\infty}, \tag{21}$$

$$\text{VHF case}: T - T_\infty = \frac{T_1}{k_f}\left(\frac{\vartheta_f}{a(1 - ct)}\right)^{1/2} x^r y^s \phi(\eta). \tag{22}$$

As an application of equation (21), we have

$$\text{VST case}: \varepsilon_3\theta'' + \Pr\left((f + g)\theta' - \left(rf' + sg'\right)\theta - S\left(\theta + \frac{\eta}{2}\theta'\right)\right) = 0,$$
$$\text{VHF case}: \varepsilon_3\phi'' + \Pr\left((f + g)\phi' - \left(rf' + sg'\right)\phi - S\left(\phi + \frac{\eta}{2}\phi'\right)\right) = 0, \tag{23}$$

with

$$\theta(0) = 1, \tag{24}$$

$$\phi'(0) = -1, \tag{25}$$

$$\theta(\infty) \longrightarrow 0, \tag{26}$$

$$\phi(\infty) \longrightarrow 0. \tag{27}$$

In equations (18)–(24), the free stream temperature is specified by T_∞, whereas (T_0, T_1) are dimensional constants. The variation in the surface temperature is controlled by the indices (r, s) along the (x, y)-directions, respectively. Thermal conductivity and specific heat capacitance are conveyed by k and ρC_p, respectively. The Prandtl number is expressed by $\Pr = (\rho C_p)_f \upsilon_f/k_f$, and the coefficient ε_3 may be expressed as

$$\varepsilon_3 = \frac{\left(\left(\left(k_{p2} + 2k_{bf}\right) + 2\psi_2\left(k_{p2} - k_{bf}\right)\right)/\left(\left(k_{p2} + 2k_{bf}\right) - \psi_2\left(k_{p2} - k_{bf}\right)\right)\right)\left(\left(\left(k_{p1} + 2k_f\right) + 2\psi_1\left(k_{p1} - k_f\right)\right)/\left(\left(k_{p1} + 2k_f\right) - \psi_1\left(k_{p1} - k_f\right)\right)\right)}{\psi_1\left(\left(\rho C_p\right)_{p1}/\left(\rho C_p\right)_f\right) + \psi_2\left(\left(\rho C_p\right)_{p2}/\left(\rho C_p\right)_f\right) + (1 - \psi_1 - \psi_2)}. \tag{28}$$

2.3. Entropy Transport. The equation that represents the entropy transport (ET) in the present situation may be expressed as

$$\mathrm{ET} = \frac{k_{\mathrm{hnf}}}{T_\infty{}^2}\left[\left(\frac{\partial T}{\partial x}\right)^2 + \left(\frac{\partial T}{\partial y}\right)^2 + \left(\frac{\partial T}{\partial z}\right)^2\right] + \frac{\sigma_{\mathrm{hnf}} B(t)^2}{T_\infty}\left[u^2 + v^2\right] + \frac{\mu_{\mathrm{hnf}}}{T_\infty}\left[\left(\frac{\partial u}{\partial z}\right)^2 + \left(\frac{\partial v}{\partial z}\right)^2\right]. \tag{29}$$

In equation (29), the first term is due to the heat transport and the second term is due to the magnetic field. It is appropriate to formulate the entropy transport as a factor form of the entropy transport (ET) rate and characteristic entropy (E_c) rate. Characteristic entropy for both the thermal regulations is defined as

$$E_{c1} = \left.\frac{k_{\mathrm{hnf}}(T_w - T_\infty)^2}{T_\infty{}^2 x^2}\right|_{\mathrm{VST\ case}}, \qquad E_{c2} = \left.\frac{k_{\mathrm{hnf}}(T - T_\infty)^2}{T_\infty{}^2 x^2}\right|_{\mathrm{VHF\ case}}. \tag{30}$$

2.3.1. Local Entropy Transport for the VST Case. The local entropy transport in dimensionless form for the VST case can be calculated as

$$\mathrm{ET}_1 = \frac{\mathrm{ET}}{E_{c1}} = \mathrm{Re}_x\theta'^2 + r^2\theta^2 + s^2\theta^2 + \frac{\mathrm{Re}_x B_r}{\alpha_1} \cdot \left[M\varepsilon_4 f'^2 + \varepsilon_5 f''^2\right] + \frac{\mathrm{Re}_y B_r}{\alpha_1}\left[M\varepsilon_4 g'^2 + \varepsilon_5 g''^2\right]. \tag{31}$$

Here, $B_r = \mu_f u_w{}^2/k_f(T_w - T_\infty)$ constitutes the Brinkman number, $\alpha_1 = (T_w - T_\infty)/T_\infty$ organizes the temperature difference parameter, and $(\varepsilon_4, \varepsilon_5)$ are due to the hybrid mixture of nanoparticles, and these may be expressed as

$$\varepsilon_4 = \frac{\left(1 + \left(3\left(\left(\sigma_{p2}/\sigma_{\mathrm{bf}}\right) - 1\right)\psi_2/\left(\left(\sigma_{p2}/\sigma_{\mathrm{bf}}\right) + 2 - \left(\left(\sigma_{p2}/\sigma_{\mathrm{bf}}\right) - 1\right)\psi_2\right)\right)\right)\left(1 + \left(3\left(\left(\sigma_{p1}/\sigma_f\right) - 1\right)\psi_1/\left(\left(\sigma_{p1}/\sigma_f\right) + 2 - \left(\left(\sigma_{p1}/\sigma_f\right) - 1\right)\psi_1\right)\right)\right)}{\left(\left(\left(k_{p2} + 2k_{\mathrm{bf}}\right) + 2\psi_2\left(k_{p2} - k_{\mathrm{bf}}\right)\right)/\left(\left(k_{p2} + 2k_{\mathrm{bf}}\right) - \psi_2\left(k_{p2} - k_{\mathrm{bf}}\right)\right)\right)\left(\left(\left(k_{p1} + 2k_f\right) + 2\psi_1\left(k_{p1} - k_f\right)\right)/\left(\left(k_{p1} + 2k_f\right) - \psi_1\left(k_{p1} - k_f\right)\right)\right)}, \tag{32}$$

$$\varepsilon_5 = \left(1 + 2.5\psi_1 + 6.2\psi_1{}^2\right)\left(1 + 2.5\psi_2 + 6.2\psi_2{}^2\right). \tag{33}$$

2.3.2. Local Entropy Transport for the VHF Case. The local entropy transport in dimensionless form for the VHF case can be calculated as

$$\mathrm{ET}_2 = \frac{\mathrm{ET}}{E_{c2}} = \mathrm{Re}_x\phi'^2 + r^2\phi^2 + s^2\phi^2 + \frac{\mathrm{Re}_x B_r}{\alpha_1}\left[M\varepsilon_4 f'^2 + \varepsilon_5 f''^2\right] + \frac{\mathrm{Re}_y B_r}{\alpha_1}\left[M\varepsilon_4 g'^2 + \varepsilon_5 g''^2\right]. \tag{34}$$

2.4. Physical Quantities. The key expressions for thermal engineering importance and heat exchanger devices are the skin friction coefficients (i.e., C_{fx} and C_{fy}) for the measurement of applied stresses at the wall, local Nusslet number (i.e., Nu_x) for the measurement of the rate of heat transference through the surface, and Bejan number (Be) for the measurement of irreversibility distribution. These engineering expressions are calculated through the following relations:

$$C_{fx} = \frac{\tau_{wx}}{\rho_f u_w{}^2}, \qquad C_{fy} = \frac{\tau_{wy}}{\rho_f v_w{}^2}, \qquad \mathrm{Nu}_x = \frac{x q_h}{k_f(T_w - T_\infty)}, \qquad \mathrm{Be} = \frac{\text{EG due to heat transfer}}{\text{Total EG}},$$

$$\tau_{wx} = \mu_{\mathrm{hnf}}\left(\frac{\partial u}{\partial z}\right)_{z=0}, \qquad \tau_{wy} = \mu_{\mathrm{hnf}}\left(\frac{\partial v}{\partial z}\right)_{z=0}, \qquad q_h = -k_{\mathrm{hnf}}\left(\frac{\partial T}{\partial z}\right)_{z=0}. \tag{35}$$

The aforementioned quantities in equations (33) and (34) utilizing Reynold's numbers $\mathrm{Re}_x = x u_w/\vartheta_f$ and $\mathrm{Re}_y = y v_w/\vartheta_f$ are expressed as

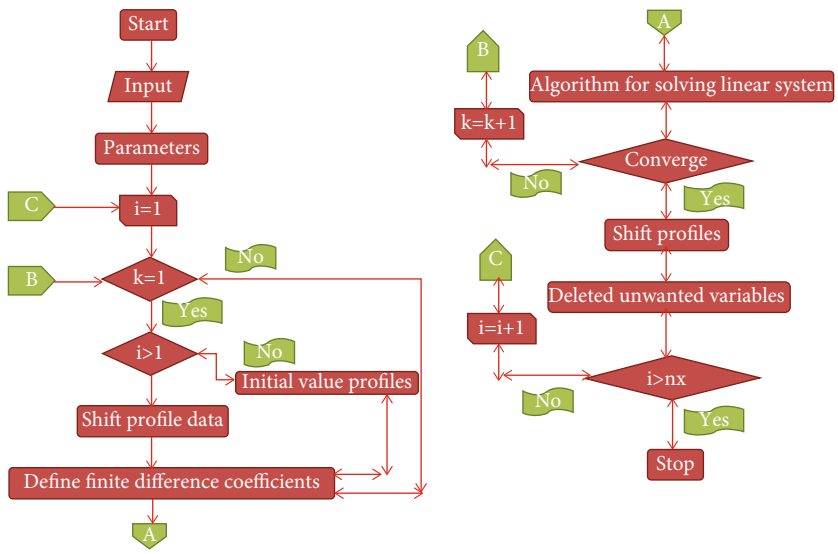

Figure 2: Flow chart for the Keller-Box simulation.

$$\mathrm{Re}_x^{1/2}C_{fx} = \varepsilon_5 f''(0),$$
$$\mathrm{Re}_y^{1/2}C_{fy} = \alpha^{-3/2}\varepsilon_5 g''(0),$$
$$\mathrm{Re}_x^{-1/2}\mathrm{Nu}_x = \begin{cases} -\dfrac{k_{\mathrm{hnf}}}{k_{\mathrm{f}}}\theta'(0) & (\text{VST case}), \\ \dfrac{k_{\mathrm{hnf}}}{k_{\mathrm{f}}}\left(\dfrac{1}{\phi(0)}\right) & (\text{VHF case}), \end{cases}$$
$$\mathrm{Be}_1|_{\mathrm{VST\ case}} = \frac{\mathrm{Re}_x\theta'^2 + r^2\theta^2 + s^2\theta^2}{\mathrm{Re}_x\theta'^2 + r^2\theta^2 + s^2\theta^2 + (\mathrm{Re}_x B_r/\alpha_1)\left[M\varepsilon_4 f'^2 + \varepsilon_5 f''^2\right] + (\mathrm{Re}_y B_r/\alpha_1)\left[M\varepsilon_4 g'^2 + \varepsilon_5 g''^2\right]},$$
$$\mathrm{Be}_2|_{\mathrm{VHF\ case}} = \frac{\mathrm{Re}_x\phi'^2 + r^2\phi^2 + s^2\phi^2}{\mathrm{Re}_x\phi'^2 + r^2\phi^2 + s^2\phi^2 + (\mathrm{Re}_x B_r/\alpha_1)\left[M\varepsilon_4 f'^2 + \varepsilon_5 f''^2\right] + (\mathrm{Re}_y B_r/\alpha_1)\left[M\varepsilon_4 g'^2 + \varepsilon_5 g''^2\right]}. \tag{36}$$

3. Keller-Box Simulation

The next task after the mathematical modeling of the physical model is to construct the solution of the modeled equations. Here, we preferred the implicit finite difference technique, namely, the Keller-Box method, for the numerical solution of the modeled equations because it has second-degree accuracy with the flexibility of step size adoption. This method is most suitable for the solution of boundary layer flow problems because of its faster convergence rate as compared to ordinary numerical approaches (i.e., shooting method, BVP4c, and RK method). By using this method, the higher-order differential equations are converted to first-order differential equations, and then the first-order differential equations are transformed into difference equations by using central difference formulae. The difference equations are converted into linearized forms by means of Newton's linearization approach, and then these equations are arranged into the matrix-vector form. The solution of the matrix-vector form of linearized equations is obtained by using the LU decomposition method. In the whole process of the numerical solution, the physical domain $[0\infty)$ is shortened to the finite domain $[\eta_0\ \eta_\infty]$ by adjusting $\eta_0 = 0$, $\eta_\infty = 20$, $n_p = 500$, and $h = (\eta_\infty - \eta_0)/n_p$ to obtain the first approximation of the numerical solution, and then the numbers of grid points n_p are increased by reducing the step size h to achieve the desired accuracy, i.e., $\varepsilon = 10^{-6}$. The complete description of the Keller-Box simulation/numerical code is presented via a flow chart (Figure 2).

Table 2: Keller-Box solution of the present mathematical model using the grid-independent approach when $\alpha = S = M = 0.5$, $r = s = 1.0$, and $\psi_1 = \psi_2 = 0.02$.

Grid points: n_p	$-f''(0)$	$-g''(0)$	$-\theta'(0)$	$\phi(0)$
500	1.423414	0.639961	3.502719	0.285493
1000	1.423413	0.639953	3.502253	0.28553
1500	1.423413	0.639952	3.502167	0.285538
2000	1.423413	0.639951	3.502137	0.28554
2500	1.423413	0.639951	3.502123	0.285541
3000	1.423413	0.639951	3.502115	0.285542
3500	1.423413	0.639951	3.50211	0.285542
4000	1.423413	0.639951	3.502107	0.285542
4500	1.423413	0.639951	3.502105	0.285542
5000	1.423413	0.639951	3.502105	0.285542
10,000	1.423413	0.639951	3.502105	0.285542

The grid-independent solution of the modeled problem via the Keller-Box method is presented in Table 2 for suitable choices of involved physical parameters with the help of thermophysical features of water, magnetite, and silver. Table 2 discloses that with the upgradation of grid points, the solution approaches its convergence criterion. 1000 grid points are enough for the convergence of $f''(0)$, 2000 grid points are enough for the convergence of $g''(0)$, 5000 grid points are sufficient for the convergence of $\theta'(0)$, and 3000 grid points are necessary for the convergence of $\phi(0)$. However, the Keller-Box solution of the mathematical model is presented with up to 10,000 grid points for the declaration of its stability. This grid-independent

Table 3: Robust validation of the present outcomes with previous investigations when $S = M = \psi_1 = \psi_2 = 0.0$.

	$f(\infty)$	$g(\infty)$	$-f''(0)$	$-g''(0)$
$\alpha = 1.0$				
Current outcomes	0.751494	0.751494	1.173721	1.173721
Liu and Andersson [27]	0.751494	0.751494	1.173721	1.173721
Wang [53]	0.751527	0.751527	1.173720	1.173720
$\alpha = 0.5$				
Current outcomes	0.842360	0.451663	1.093096	0.465206
Liu and Andersson [27]	0.842360	0.451663	1.093096	0.465206
Wang [53]	0.842360	0.451671	1.093097	0.465205
$\alpha = 0.0$				
Current outcomes	1.0	0.0	-1.0	0.0
Liu and Andersson [27]	1.0	0.0	-1.0	0.0
Wang [53]	1.0	0.0	-1.0	0.0

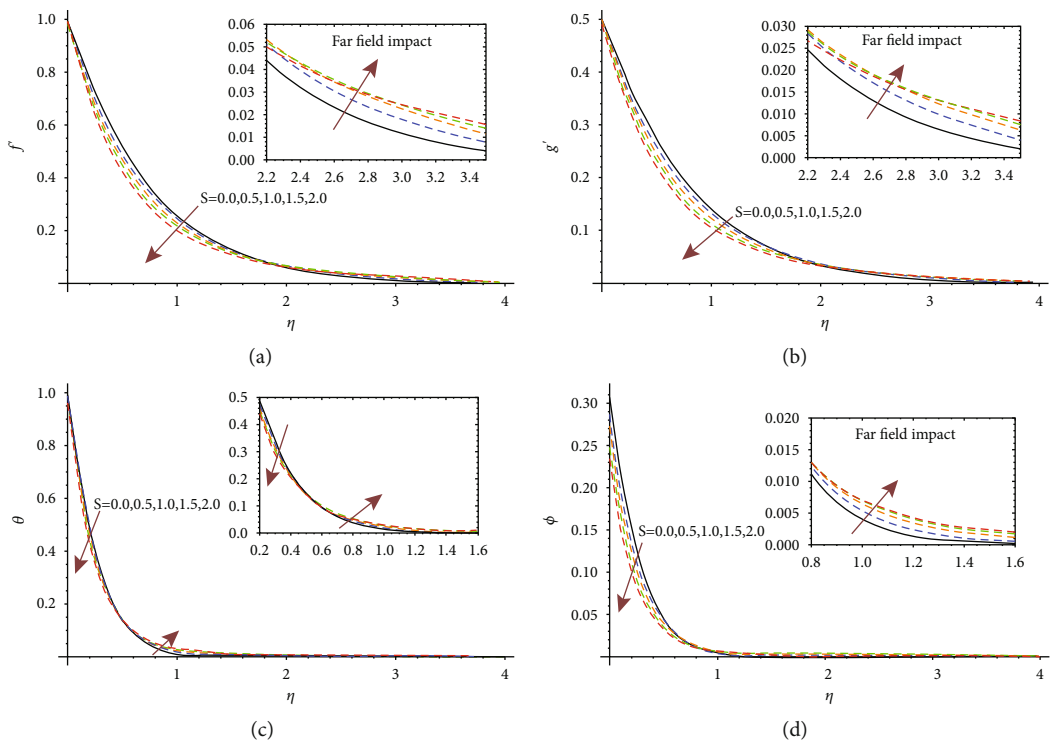

Figure 3: (a–d) The impact of the unsteady factor on $f'(\eta)$ via panel (a), on $g'(\eta)$ via panel (b), on $\theta(\eta)$ via panel (c), and on $\phi(\eta)$ via panel (d).

solution is further used to manipulate the outcomes for physical quantities of thermal importance and for graphical illustrations against various choices of pertinent involved entities.

3.1. Robust Validation. In order to the validation of the numerical technique using the grid-independent approach, a restricted comparison is incorporated with the existing literature by using 10,000 grid points in Table 3. A convincing pact is found among current scrutiny and previous investigations.

4. Results and Discussion

The major and foremost outcomes of the present investigation are discussed in this section of the report in the form of tables and various graphical representations. The impact of unsteady factor S on hybrid nanofluid velocity component $f'(\eta)$, velocity component $g'(\eta)$, thermal setup $\theta(\eta)$ for the VST environment, and thermal setup $\phi(\eta)$ for the VHF environment is discussed through Figures 3(a)–3(d), respectively. It is observed through Figures 3(a)–3(d) that the progression in the choice of

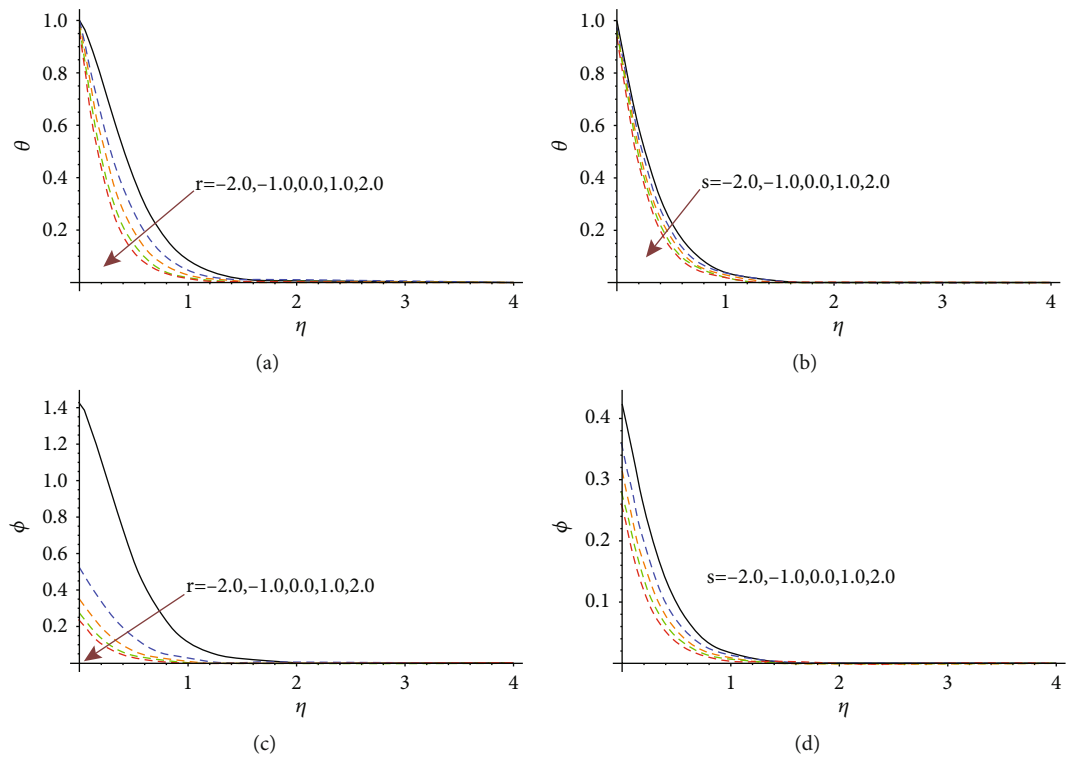

Figure 4: (a–d) Impacts of indices r on $\theta(\eta)$ via panel (a), s on $\theta(\eta)$ via panel (b), r on $\phi(\eta)$ via panel (c), and s on $\phi(\eta)$ via panel (d).

the unsteady factor from $S = 0.0 - 2.0$ reduces the impact of velocities f' and g', impact of thermal setup $\theta(\eta)$ for the VST approach, and impact of thermal setup $\phi(\eta)$ for the VHF approach nearer to the stretching device. Opposite trends are noticed in the far-field environment. Physically, the unsteady factor is the ratio of the dimensional constant c to the expansion rate a, and thus, the escalation in the choice of S produces a lower expansion rate and enhances the impact of c (i.e., positive expansion). Mathematically, the unsteady factor is also involved in the modeled equations in the product form with the quantities $f'(\eta)$, $g'(\eta)$, $\theta(\eta)$, and $\phi(\eta)$, respectively. As a result, these quantities are reduced with the escalation in the choice of the unsteady factor nearer to the stretching device. Moreover, the thickness of the boundary stream is also reduced with the improvement in the choice of the unsteady factor.

The significance of temperature-controlling indices r and s on the thermal setup is discussed in Figures 4(a) and 4(b) for the VST environment and Figures 4(c) and 4(d) for the VHF environment. It is noticed through these figures that intensifying choices of r and s diminish the thermal setup for both the prescribed heating mechanisms. Physically, r and s are involved in the energy equation as the product of $\theta(\eta)$ and $\phi(\eta)$, that is, the main cause of temperature reduction. Moreover, negative choices of r and s produce more temperature distribution than positive choices of r and s. Furthermore, the temperature distribution is activated higher for the VHF environment than the VST environment for $r = -2$, whereas it is triggered higher for VST aspects than VHF aspects for all the adopted choices of the index s. The augmentation in the choice of r reduces the thickness of the thermal layer, and the thickness of the thermal layer dominates for the diverse considerations of r than the considerations of s (i.e., thermal index along the y-direction). Figure 5(a) accompanies the significance of M and implication of α on $f'(\eta)$. The first velocity component $f'(\eta)$ is abbreviated with the enlargement of M from $M = 0.0 - 1.6$ and amplification of α for $\alpha = 0.4$ and $\alpha = 0.7$ (i.e., dashed lines). Physically, the stretching rate a lies in the denominator of both factors M and α, and therefore, the reduction to $f'(\eta)$ can be observed.

Figure 5(b) conveys the importance of M and inference of α on $g'(\eta)$. The second velocity component $g'(\eta)$ is abridged with the development of M from $M = 0.0 - 1.6$, and it is enhanced with the magnification of α for $\alpha = 0.4$ and $\alpha = 0.7$ (i.e., dashed lines). Physically, the stretching rate b lies in the numerator of α, whereas the stretching rate a deceits in the denominator of M (i.e., magnetic parameter). Therefore, the proliferation in $g'(\eta)$ is noticed for α and reduction in $g'(\eta)$ is observed for the magnetic factor. The thickness of the momentum layer is also improved due to the resistivity impact of the Lorentz force. Figure 5(c) illustrates the consequence of M and significance of α on $\theta(\eta)$. Temperature $\theta(\eta)$ is condensed with the progression of α, whereas it is intensified with the evolution of the magnetic factor. Physically, the Lorentz force slows down the velocity of the hybrid nanofluid and gave the domination chance to $\theta(\eta)$ (i.e., temperature for the VST process). Figure 5(d) elucidates the importance of M and worth of α on $\phi(\eta)$. Temperature $\phi(\eta)$ is shortened with the evolution of α, whereas it is deepened with the advancement of the magnetic feature. Actually, the Lorentz force acts as a resistive agent for

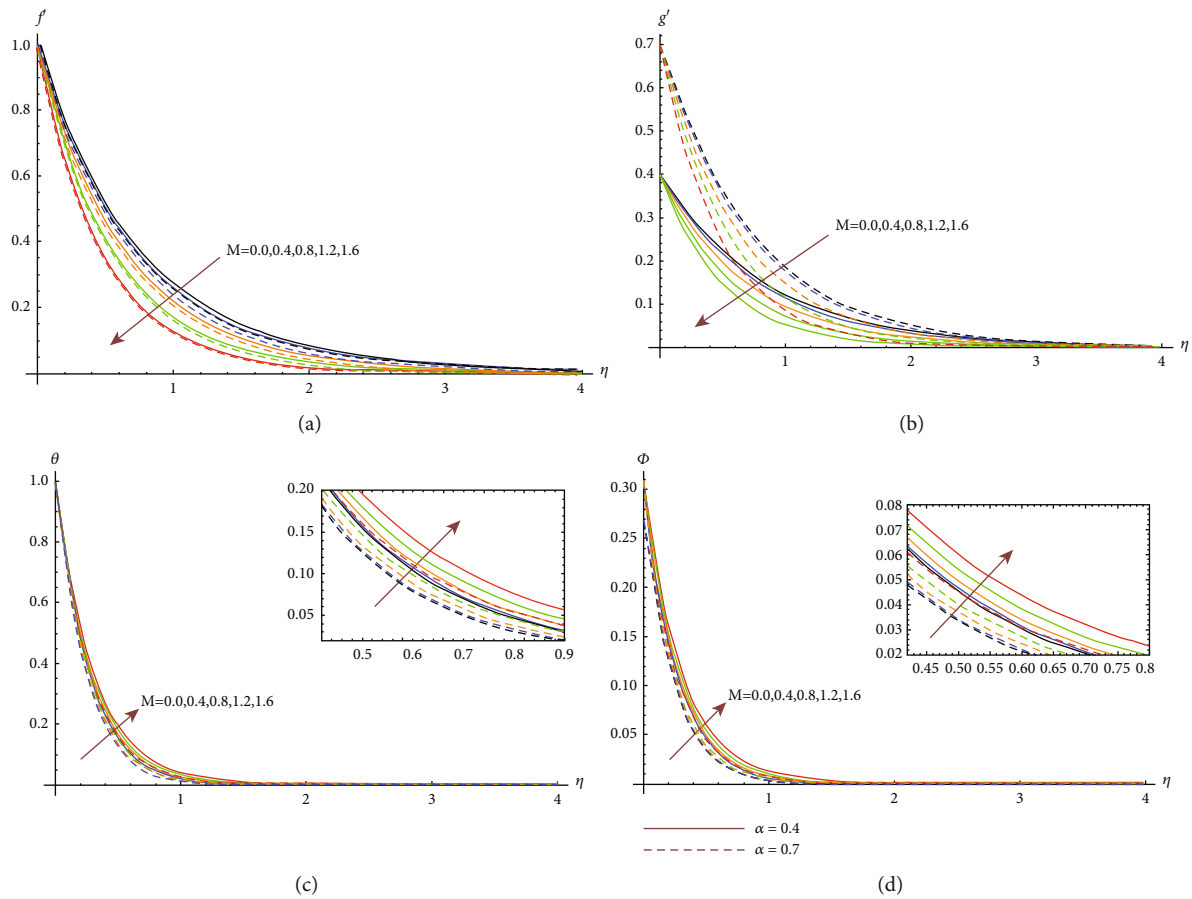

Figure 5: (a–d) Impacts of M and α on $f'(\eta)$ via panel (a), on $g'(\eta)$ via panel (b), on $\theta(\eta)$ via panel (c), and on $\phi(\eta)$ via panel (d).

Table 4: Significance of nanoparticle volume fractions ψ_1 and ψ_2 on the physical quantities having thermal engineering interests when $\alpha = S = M = 0.5$ and $r = s = 1.0$.

Nanoparticle volume fractions		$-\mathrm{Re}_y^{1/2} C_{fx}$	$-\mathrm{Re}_y^{1/2} C_{fy}$	$\mathrm{Re}_x^{-1/2} \mathrm{Nu}_x$
ψ_1	ψ_2			
0.01	0.01	1.456536	1.853745	3.855186
0.03	0.01	1.54797	1.969733	3.903703
0.05	0.01	1.643119	2.090527	3.951304
0.07	0.01	1.742064	2.216231	3.997992
0.07	0.03	1.898586	2.412816	4.046919
0.07	0.05	2.058013	2.613309	4.094455
0.07	0.07	2.221041	2.818552	4.140588

the velocity of the hybrid mixture, and hence, $\phi(\eta)$ is increased with its positive approach.

Table 4 provides the significance of magnetite tiny particle volume fraction ψ_1 and silver tiny particle volume fraction ψ_2 on the skin friction coefficients and local Nusslet number for fixed choices of other involved entities. It is elaborated in Table 4 that higher choices of ψ_1 and ψ_2

Table 5: Variation in the thermophysical features for the present mixture of substances with $\psi_1 = 0.01$.

ψ_2	ρ_{hnf}	$(\rho C_p)_{\mathrm{hnf}} \times 10^3$	$k_{\mathrm{hnf}} \times 10^{-1}$	$\sigma_{\mathrm{hnf}} \times 10^{-2}$
0.00	1038.929	4.14391	6.284229742	5.151514233
0.01	1133.958	4.10447	6.473818137	5.307620725
0.03	1324.016	4.02559	6.864669077	5.629489779
0.05	1514.074	3.94671	7.271901012	5.964911215
0.07	1704.132	3.86783	7.696565802	6.31475938
0.09	1894.19	3.78895	8.139807334	6.679985485

Table 6: Variation in the thermophysical features for the present mixture of substances with $\psi_2 = 0.01$.

ψ_1	ρ_{hnf}	$(\rho C_p)_{\mathrm{hnf}} \times 10^3$	$k_{\mathrm{hnf}} \times 10^{-1}$	$\sigma_{\mathrm{hnf}} \times 10^{-2}$
0.00	1092.129	4.13956	6.31495557	5.151515151
0.01	1133.958	4.10447	6.473818137	5.307620725
0.03	1217.616	4.03429	6.799670393	5.629487827
0.05	1301.274	3.96411	7.136828795	5.964907143
0.07	1384.932	3.89393	7.485892168	6.134753003
0.09	1468.59	3.82375	7.487502391	6.679976602

Table 7: Percent-wise heat transport calculation for the various possessions of nanoparticles, $\alpha = S = M = 0.5$ and $r = s = 1.0$, by using the following formulae, i.e., %Increase = ((With nanoparticles − Without nanoparticles)/Without nanoparticles) × 100 = Result and % Enhancement = Result − 100%.

ψ_1, ψ_2	$Re_x^{-1/2}Nu_x$	
	$Fe_3O_4(\psi_2 = 0.0)$	$Ag(\psi_1 = 0.0)$
0.00	3.789531	3.789531
0.01	3.813768 (0.6395778% increase)	3.814161 (0.6499485% increase)
0.02	3.837764 (1.272796% increase)	3.838539 (1.2932471% increase)
0.04	3.885047 (2.520523% increase)	3.886515 (2.5592613% increase)
0.06	3.931391 (3.7434712% increase)	3.933425 (3.7971453% increase)
0.08	3.976797 (4.9416669% increase)	3.979245 (5.0062659% increase)

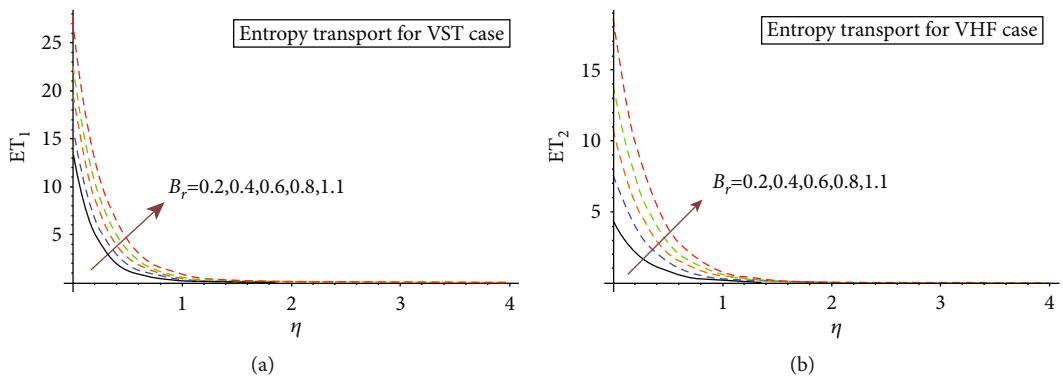

Figure 6: (a, b) Entropy transport for the variation of the Brinkman number.

enhance the worth of skin friction coefficients. Mathematically, the skin friction coefficients consist of the factor of tiny particle volume fractions, and therefore, strictly increasing behavior in the amount of skin friction is achieved with the development of volume fractions of tiny particles. Moreover, the skin friction coefficient is detected higher for the y-direction as compared to the x-direction as its mathematical expression involves the term of expansion ratio α with negative fraction power. The rate of heat transference is increased for both $0.01 \leq \psi_1 \leq 0.07$ and $0.01 \leq \psi_2 \leq 0.07$. Physically, the rate of heat transference depends on the value of thermal conductivity for magnetite and silver nanoparticles. As the thermal conductivity is higher for silver, silver is higher than magnetite, and therefore, silver nanoparticles have produced a faster rate of heat transference as compared to magnetite nanoparticles. Table 5 provides the impact of volume fraction ψ_2 on the thermophysical features of hybrid nanofluid with the present mixture of the substances, whereas Table 6 discloses the effect of volume fraction ψ_1 on the thermophysical features of hybrid nanofluid with the mixture of water, magnetite, and silver. It is noticed through these tables that higher choices of ψ_1 and ψ_2 reduce the effective heat capacity of hybrid nanofluid, whereas the escalating amounts of these substances (magnetite and silver) boost the worth of thermal conductivity, density, and electrical conductivity of the hybrid nanofluid. These outcomes are favorable for a lot of industrial and engineering applications. Table 7 is included to discuss the percentage increase in the rate of heat transport for the suspensions of magnetite and silver in the host liquid, i.e., water. According to the calculated results, silver is more reliable and efficient in order to enhance the rate of heat transport than magnetite. Physically, the thermal conductivity of silver is much higher than that of magnetite, and so the percent-wise enhancement in the rate of heat transport is observed to be higher for silver nanoparticles.

Figure 6(a) is included to discuss the control of Brinkman number B_r on entropy transport for the VST case, whereas Figure 6(b) illustrates its impact on entropy transport for the VHF case. Entropy is augmented with the upgradation of B_r from $B_r = 0.2 - 1.1$, and the worth of this augmentation is almost doubled for the VST case as compared to the VHF case. Physically, the velocity of the fluid enhances with the progression of B_r and declines with the augmentation of the temperature difference between the wall and the far-field. So, these spectacular trends are achieved with the variation of the Brinkman number. Figure 7(a) is incorporated to confer the influence of temperature difference parameter α_1 on the Bejan number for the VST case, whereas Figure 7(b) elucidates its impression on the Bejan number for the VHF case. The Bejan number is amplified with the evolution of α_1 from $\alpha_1 = 0.1 - 0.9$, and the net impact of this intensification is almost doubled for the VST case as compared to the VHF case. Physically, the far-field temperature contracts with the advancement of α_1 and amplifies with the growth of the temperature difference between the wall and the far-field. So, these enormous tendencies are attained with the variant of the temperature difference parameter.

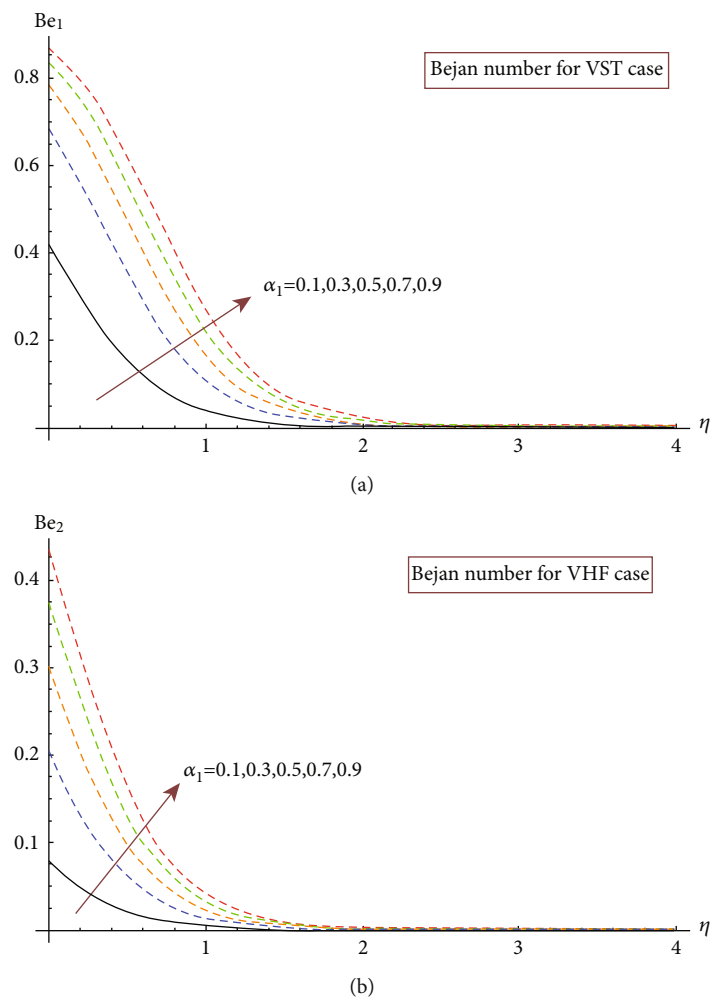

Figure 7: (a, b) Bejan number for the variation of the temperature difference parameter.

5. Conclusions

Heat transport and entropy transport in bidirectional hybrid nanofluid containing nanospheres (magnetite and silver) with VST (variable surface temperature) and VHF (variable surface heat flux) mechanisms are scrutinized. The Hamilton-Crosser nanofluid model is used to inspect the impact of nanospheres. Water is considered the base fluid with the amalgamations of nanospheres. The Keller-Box method has been used to solve the modeled problem, and outcomes have been discussed graphically as well as in tabular arrangements. The pertinent observations are as follows:

(i) The velocity setup for the present mixture of nanospheres into the host liquid remains on the inferior side

(ii) The reduction in the thermal setup has been chronicled for the amplification in the choices of heat distribution indices

(iii) The Nusselt number for the present combination of nanospheres shows its proficiency for escalating nanosphere volume fractions

(iv) The nanospheres play a vital role in the improvement of the thermal conductivity of hybrid nanofluid

(v) Percentage enhancement in the rate of heat transport is observed to be higher for silver nanospheres as compared to magnetite nanospheres

(vi) Entropy is amplified with the positive estimation of the Brinkman number, and the Bejan number is also amplified with the positive tendency of the temperature difference parameter

The outcomes of the present investigation are helpful in the development of heat exchangers, coating a sheet with nanoparticles, the purification process of water, steel manufacturing, drug delivery, etc.

Nomenclature

(x, y, z):	Cartesian configuration
(u, v, w):	Velocity field components
t:	Time
T:	Temperature

η:	Similarity variable
(f, g, θ):	Similarity functions
(r, s):	Indices
Pr:	Prandtl number
ET:	Entropy transport
E_c:	Characteristic entropy
VST:	Variable surface temperature
ET_1:	Entropy for the VST case
VHF:	Variable surface heat flux
ET_2:	Entropy for the VHF case
(a, b):	Stretching rates
c:	Positive constant
B_0:	Magnetic field strength
(u_w, v_w):	Stretching velocities
H_2O:	Water
Fe_3O_4:	Magnetite
Ag:	Silver
ρ:	Density
k:	Thermal conductivity
C_p:	Specific heat
σ:	Electrical conductivity
μ:	Dynamic viscosity
bf:	Base fluid
hnf:	Hybrid nanofluid
ψ_1:	Concentration of magnetite nanospheres
ψ_2:	Concentration of silver nanospheres
ϑ_f:	Kinematic viscosity of fluid
S:	Unsteady parameter
M:	Magnetic parameter
α:	Bidirectional stretching parameter
$\varepsilon_i, i = 1 - 5$:	Hybrid nanofluid coefficients
q_w:	Heat flux
(T_0, T_1):	Dimensional constants
T_w:	Surface temperature
(Re_x, Re_y):	Reynold's numbers
T_∞:	Ambient temperature
B_r:	Brinkman number
α_1:	Temperature difference parameter
(C_{fx}, C_{fy}):	Skin friction coefficients
Nu_x:	Nusselt number
(Be_1, Be_2):	Bejan numbers
h:	Step size
ε:	Convergence criterion.

Data Availability

The raw data supporting the conclusion of this report will be made available by the corresponding author without undue reservation.

Conflicts of Interest

The authors declare that there is no conflict of interest.

Authors' Contributions

All authors contributed equally to this work. And all the authors have read and approved the final version manuscript.

References

[1] S. U. S. Choi, Z. G. Zhang, W. Yu, F. E. Lockwood, and E. A. Grulke, "Anomalous thermal conductivity enhancement in nanotube suspensions," *Applied Physics Letters*, vol. 79, no. 14, pp. 2252–2254, 2001.

[2] J. C. Maxwell, *A Treatise on Electricity and Magnetism (Vol. 1)*, Clarendon Press, Oxford, 1873.

[3] V. D. Bruggeman, "Berechnung verschiedener physikalischer Konstanten von heterogenen Substanzen. I. Dielektrizitätskonstanten und Leitfähigkeiten der Mischkörper aus isotropen Substanzen," *Annalen der Physik*, vol. 416, no. 7, pp. 636–664, 1935.

[4] R. L. Hamilton and O. K. Crosser, "Thermal conductivity of heterogeneous two-component systems," *Industrial & Engineering Chemistry Fundamentals*, vol. 1, no. 3, pp. 187–191, 1962.

[5] N. Masoumi, N. Sohrabi, and A. Behzadmehr, "A new model for calculating the effective viscosity of nanofluids," *Journal of Physics D: Applied Physics*, vol. 42, no. 5, article 055501, 2009.

[6] M. Mooney, "The viscosity of a concentrated suspension of spherical particles," *Journal of Colloid Science*, vol. 6, no. 2, pp. 162–170, 1951.

[7] H. Ohshima, "Effective viscosity of a concentrated suspension of uncharged spherical soft particles," *Langmuir*, vol. 26, no. 9, pp. 6287–6294, 2010.

[8] X. Zhang, H. Gu, and M. Fujii, "Effective thermal conductivity and thermal diffusivity of nanofluids containing spherical and cylindrical nanoparticles," *Journal of Applied Physics*, vol. 100, no. 4, article 044325, 2006.

[9] S. Saleem, I. L. Animasaun, S. J. Yook, Q. M. Al-Mdallal, N. A. Shah, and M. Faisal, "Insight into the motion of water conveying three kinds of nanoparticles shapes on a horizontal surface: significance of thermo-migration and Brownian motion," *Surfaces and Interfaces*, vol. 30, article 101854, 2022.

[10] E. V. Timofeeva, J. L. Routbort, and D. Singh, "Particle shape effects on thermophysical properties of alumina nanofluids," *Journal of Applied Physics*, vol. 106, no. 1, article 014304, 2009.

[11] K. Yang and Y. Q. Ma, "Computer simulation of the translocation of nanoparticles with different shapes across a lipid bilayer," *Nature Nanotechnology*, vol. 5, no. 8, pp. 579–583, 2010.

[12] I. Ahmad, M. Faisal, Q. Zan-Ul-Abadin, T. Javed, and K. Loganathan, "Unsteady 3D heat transport in hybrid nanofluid containing brick shaped ceria and zinc-oxide nanocomposites with heat source/sink," *Nano*, vol. 8, no. 1, pp. 1–12, 2022.

[13] S. S. U. Devi and S. A. Devi, "Numerical investigation of three-dimensional hybrid Cu–Al_2O_3/water nanofluid flow over a stretching sheet with effecting Lorentz force subject to Newtonian heating," *Canadian Journal of Physics*, vol. 94, no. 5, pp. 490–496, 2016.

[14] T. Hayat, S. Nadeem, and A. U. Khan, "Rotating flow of Ag-CuO/H_2O hybrid nanofluid with radiation and partial slip boundary effects," *The European Physical Journal E*, vol. 41, no. 6, pp. 1–9, 2018.

[15] V. Kumar and R. R. Sahoo, "Viscosity and thermal conductivity comparative study for hybrid nanofluid in binary base fluids," *Research*, vol. 48, no. 7, pp. 3144–3161, 2019.

[16] M. F. Nabil, W. H. Azmi, K. A. Hamid, N. N. M. Zawawi, G. Priyandoko, and R. Mamat, "Thermo-physical properties of hybrid nanofluids and hybrid nanolubricants: a comprehensive review on performance," *International Communications in Heat and Mass Transfer*, vol. 83, pp. 30–39, 2017.

[17] U. Rashid and H. Liang, "Investigation of nanoparticles shape effects on MHD nanofluid flow and heat transfer over a rotating stretching disk through porous medium," *International Journal of Numerical Methods for Heat & Fluid Flow*, vol. 30, no. 12, pp. 5169–5189, 2020.

[18] H. A. Nabwey and A. Mahdy, "Transient flow of micropolar dusty hybrid nanofluid loaded with Fe_3O_4-Ag nanoparticles through a porous stretching sheet," *Results in Physics*, vol. 21, article 103777, 2021.

[19] N. A. Zainal, R. Nazar, K. Naganthran, and I. Pop, "Heat generation/absorption effect on MHD flow of hybrid nanofluid over bidirectional exponential stretching/shrinking sheet," *Chinese Journal of Physics*, vol. 69, pp. 118–133, 2021.

[20] N. Ahmed, F. Saba, U. Khan et al., "Spherical shaped (Ag $-Fe_3O_4/H_2O$) hybrid nanofluid flow squeezed between two Riga plates with nonlinear thermal radiation and chemical reaction effects," *Energies*, vol. 12, no. 1, pp. 1–23, 2019.

[21] G. Sowmya, B. J. Gireesha, I. L. Animasaun, and N. A. Shah, "Significance of buoyancy and Lorentz forces on water-conveying iron(III) oxide and silver nanoparticles in a rectangular cavity mounted with two heated fins: heat transfer analysis," *Journal of Thermal Analysis and Calorimetry*, vol. 144, no. 6, pp. 2369–2384, 2021.

[22] N. Acharya, F. Mabood, and I. A. Badruddin, "Thermal performance of unsteady mixed convective Ag/MgO nanohybrid flow near the stagnation point domain of a spinning sphere," *International Communications in Heat and Mass Transfer*, vol. 134, article 106019, 2022.

[23] F. Ali, K. Loganathan, S. Eswaramoorthi, K. Prabu, A. Zaib, and D. K. Chaudhary, "Heat transfer analysis on carboxymethyl cellulose water-based cross hybrid nanofluid flow with entropy generation," *Journal of Nanomaterials*, vol. 2022, Article ID 5252918, 11 pages, 2022.

[24] K. Thriveni and B. Mahanthesh, "Sensitivity computation of nonlinear convective heat transfer in hybrid nanomaterial between two concentric cylinders with irregular heat sources," *International Communications in Heat and Mass Transfer*, vol. 129, article 105677, 2021.

[25] J. Mackolil and B. Mahanthesh, "Optimization of heat transfer in the thermal Marangoni convective flow of a hybrid nanomaterial with sensitivity analysis," *Applied Mathematics and Mechanics*, vol. 42, no. 11, pp. 1663–1674, 2021.

[26] J. L. G. Oliveira, C. Tecchio, K. V. Paiva, M. B. H. Mantelli, R. Gandolfi, and L. G. S. Ribeiro, "Passive aircraft cooling systems for variable thermal conditions," *Applied Thermal Engineering*, vol. 79, pp. 88–97, 2015.

[27] I. C. Liu and H. I. Andersson, "Heat transfer over a bidirectional stretching sheet with variable thermal conditions," *International Journal of Heat and Mass Transfer*, vol. 51, no. 15-16, pp. 4018–4024, 2008.

[28] I. Ahmad, M. Faisal, and T. Javed, "Dynamics of copper–water nanofluid with the significance of prescribed thermal conditions," *Heat Transfer*, vol. 50, no. 5, pp. 4248–4263, 2021.

[29] I. Ahmad, M. Faisal, and T. Javed, "Unsteady rotating flow of nanofluid with prescribed thermal aspects," *International Journal of Modern Physics C*, vol. 32, no. 7, article 2150093, 2021.

[30] I. Waini, A. Ishak, and I. Pop, "Hybrid nanofluid flow on a shrinking cylinder with prescribed surface heat flux," *International Journal of Numerical Methods for Heat & Fluid Flow*, vol. 31, no. 6, pp. 1987–2004, 2021.

[31] I. Waini, A. Ishak, and I. Pop, "Hybrid nanofluid flow and heat transfer past a vertical thin needle with prescribed surface heat flux," *International Journal of Numerical Methods for Heat & Fluid Flow*, vol. 29, no. 12, pp. 4875–4894, 2019.

[32] N. S. Khashi'ie, I. Waini, N. A. Zainal, K. Hamzah, and A. R. Mohd Kasim, "Hybrid nanofluid flow past a shrinking cylinder with prescribed surface heat flux," *Symmetry*, vol. 12, no. 9, p. 1493, 2020.

[33] B. J. Gireesha, B. Mahanthesh, and R. S. R. Gorla, "Suspended particle effect on nanofluid boundary layer flow past a stretching surface," *Journal of Nanofluids*, vol. 3, no. 3, pp. 267–277, 2014.

[34] I. Ahmad, M. Faisal, and T. Javed, "Bi-directional stretched nanofluid flow with Cattaneo-Christov double diffusion," *Results in Physics*, vol. 15, article 102581, 2019.

[35] T. Javed, M. Faisal, and I. Ahmad, "Dynamisms of solar radiation and prescribed heat sources on bidirectional flow of magnetized Eyring-Powell nanofluid," *Case Studies in Thermal Engineering*, vol. 21, article 100689, 2020.

[36] M. Turkyilmazoglu and I. Pop, "Heat and mass transfer of unsteady natural convection flow of some nanofluids past a vertical infinite flat plate with radiation effect," *International Journal of Heat and Mass Transfer*, vol. 59, pp. 167–171, 2013.

[37] T. Javed, M. Faisal, and I. Ahmad, "Dynamisms of activation energy and convective Nield's conditions on bidirectional flow of radiative Eyring–Powell nanofluid," *International Journal of Modern Physics C (IJMPC)*, vol. 31, no. 11, article 2050156, 2020.

[38] G. Huminic and A. Huminic, "Entropy generation of nanofluid and hybrid nanofluid flow in thermal systems: a review," *Journal of Molecular Liquids*, vol. 302, article 112533, 2020.

[39] M. I. Khan, M. U. Hafeez, T. Hayat, M. I. Khan, and A. Alsaedi, "Magneto rotating flow of hybrid nanofluid with entropy generation," *Computer Methods and Programs in Biomedicine*, vol. 183, article 105093, 2020.

[40] G. Huminic and A. Huminic, "The heat transfer performances and entropy generation analysis of hybrid nanofluids in a flattened tube," *International Journal of Heat and Mass Transfer*, vol. 119, pp. 813–827, 2018.

[41] S. Ahmad, S. Nadeem, and N. Ullah, "Entropy generation and temperature-dependent viscosity in the study of SWCNT–MWCNT hybrid nanofluid," *Applied Nanoscience*, vol. 10, no. 12, pp. 5107–5119, 2020.

[42] U. M. Zahid, Y. Akbar, and F. M. Abbasi, "Entropy generation analysis for peristaltically driven flow of hybrid nanofluid," *Chinese Journal of Physics*, vol. 67, pp. 330–348, 2020.

[43] A. A. Hussien, M. Z. Abdullah, N. M. Yusop, W. Al-Kouz, E. Mahmoudi, and M. Mehrali, "Heat transfer and entropy generation abilities of MWCNTs/GNPs hybrid nanofluids in microtubes," *Entropy*, vol. 21, no. 5, p. 480, 2019.

[44] M. Sheikholeslami, Z. Shah, A. Shafee, P. Kumam, and H. Babazadeh, "Lorentz force impact on hybrid nanofluid within a porous tank including entropy generation," *International Communications in Heat and Mass Transfer*, vol. 116, article 104635, 2020.

[45] H. Upreti, A. K. Pandey, and M. Kumar, "Assessment of entropy generation and heat transfer in three-dimensional

hybrid nanofluids flow due to convective surface and base fluids," *Journal of Porous Media*, vol. 24, no. 3, pp. 35–50, 2021.

[46] B. Saleh and L. S. Sundar, "Entropy generation and exergy efficiency analysis of ethylene glycol-water based nanodiamond + Fe_3O_4 hybrid nanofluids in a circular tube," *Powder Technology*, vol. 380, pp. 430–442, 2021.

[47] S. Eswaramoorthi, S. Divya, M. Faisal, and N. Namgyel, "Entropy and heat transfer analysis for MHD flow of-water-based nanofluid on a heated 3D plate with nonlinear radiation," *Mathematical Problems in Engineering*, vol. 2022, Article ID 7319988, 14 pages, 2022.

[48] M. Faisal, I. Ahmad, and T. Javed, "Keller-Box simulation for nonzero and zero mass fluxes of nanofluid flow impinging over a bi-directional stretching sheet: an unsteady mathematical model," *International Journal of Modern Physics C*, vol. 32, no. 4, article 2150052, 2021.

[49] I. Ahmad, M. Faisal, and T. Javed, "Magneto-nanofluid flow due to bidirectional stretching surface in a porous medium," *Special Topics & Reviews in Porous Media: An International Journal*, vol. 10, no. 5, pp. 457–473, 2019.

[50] M. Faisal, I. Ahmad, and T. Javed, "Radiative nanofluid flow due to unsteady bi-directional stretching surface with convective and zero mass flux boundary conditions: using Keller Box scheme," *Computational Thermal Sciences: An International Journal*, vol. 12, no. 4, pp. 361–385, 2020.

[51] T. Javed, M. Faisal, and I. Ahmad, "Actions of viscous dissipation and ohmic heating on bidirectional flow of a magneto-Prandtl nanofluid with prescribed heat and mass fluxes," *Heat Transfer*, vol. 49, no. 8, pp. 4801–4819, 2020.

[52] M. Faisal, I. Ahmad, and T. Javed, "Numerical simulation of mixed convective 3D flow of a chemically reactive nanofluid subject to convective Nield's conditions with a nonuniform heat source/sink," *Heat Transfer*, vol. 50, no. 1, pp. 352–369, 2021.

[53] C. Y. Wang, "The three-dimensional flow due to a stretching flat surface," *The Physics of Fluids*, vol. 27, no. 8, pp. 1915–1917, 1984.